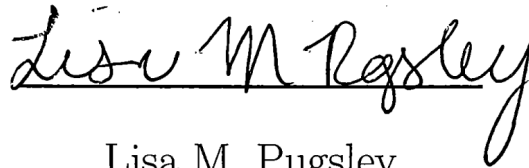


Extraordinary Magnetoresistance in Two and Three Dimensions: Geometrical Optimization

BY



Lisa M. Pugsley

A THESIS

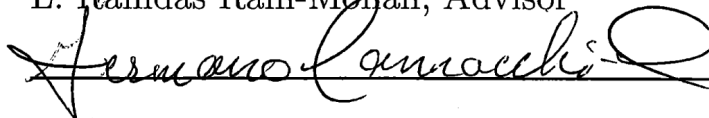
SUBMITTED TO THE FACULTY OF
WORCESTER POLYTECHNIC INSTITUTE
IN PARTIAL FULFILLMENT OF THE REQUIREMENTS
FOR THE DEGREE OF MASTER OF SCIENCE
IN PHYSICS

Submitted: April 2012

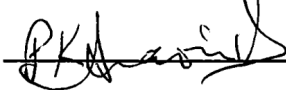
Approved:



L. Ramdas Ram-Mohan, Advisor



Germano S. Iannacchione, Department Head



Padmanabhan K. Aravind, Associate Department Head

Abstract

The extraordinary magnetoresistance (EMR) in metal-semiconductor hybrid structures was first demonstrated using a van der Pauw configuration for a circular semiconductor wafer with a concentric metallic inclusion in it. This effect depends on the orbital motion of carriers in an external magnetic field, and the remarkably high magnetoresistance response observed suggests that the geometry of the metallic inclusion can be optimized to significantly enhance the EMR. Here we consider the theory and simulations to achieve this goal by comparing both two-dimensional as well as three-dimensional structures in an external magnetic field to evaluate the EMR in them. Examples of structures that are compatible with present day technological capabilities are given together with their expected responses in terms of EMR. For a 10 micron 2D square structure with a square metallic inclusion, we see a MR up to 10^7 percent for an applied magnetic field of 1 Tesla.

CONTENTS

List of Figures	iii
I. Introduction	1
II. Theoretical Considerations	2
A. The Action Integral	3
B. The Finite Element Method with \mathcal{C}_1 -continuous Elements	5
C. Boundary Conditions for Hermite Elements	6
III. The Magnetoresistance	8
A. A Rectangular Metallic Region Embedded in a Semiconductor	8
1. $10\ \mu\text{m}$, Centered Ports	9
2. $10\ \mu\text{m}$, Diagonal Ports	9
3. $10\ \mu\text{m}$, Ports IVIV	9
4. $10\ \mu\text{m}$, Ports IVVI	10
5. $300\ \text{nm}$, Centered Ports	10
B. Circular Metallic Region Embedded in a Semiconductor	10
C. Multiple Metallic Regions Embedded in a 2D Semiconductor Wafer	11
1. Multiple Regions with Current Ports along x	11
2. Multiple Regions with Current Ports along y	11
D. Metallic Cube Embedded in a 3D Semiconductor Cube	12
IV. Concluding Remarks	13
Acknowledgments	14
References	52

LIST OF FIGURES

1	A 2D Reference Element.....	15
2	Matrix Manipulation for Setting Two Nodal Values to be the Same.....	16
3	A Semiconductor Wafer with a Rectangular Metallic Inclusion.....	17
4	A schematic for a $10\ \mu\text{m}$ Square with Ports Centered on all Sides.....	18
5	Potential and Current for a $10\ \mu\text{m}$ Square with Centered Ports for $B = -1\ \text{T}$	18
6	Potential and Current for a $10\ \mu\text{m}$ Square with Centered Ports for $B = 0\ \text{T}$..	19
7	Potential and Current for a $10\ \mu\text{m}$ Square with Centered Ports for $B = 1\ \text{T}$..	19
8	Resistance Versus Magnetic Field for a $10\ \mu\text{m}$ Square with Centered Ports ...	20
9	Magnetoresistance Versus Magnetic Field for a $10\ \mu\text{m}$ Square with Centered Ports	21
10	A schematic for a $10\ \mu\text{m}$ Square with Diagonal Ports	22
11	Potential and Current for a $10\ \mu\text{m}$ Square with Diagonal Ports for $B = -1\ \text{T}$	22
12	Potential and Current for a $10\ \mu\text{m}$ Square with Diagonal Ports for $B = 0\ \text{T}$..	23
13	Potential and Current for a $10\ \mu\text{m}$ Square with Diagonal Ports for $B = 1\ \text{T}$..	23
14	Resistance Versus Magnetic Field for a $10\ \mu\text{m}$ Square with Diagonal Ports ...	24
15	Magnetoresistance Versus Magnetic Field for a $10\ \mu\ \text{m}$ Square with Diagonal Ports	24
16	A schematic for a $10\ \mu\text{m}$ Square with Ports IVIV.....	25
17	Potential and Current for a $10\ \mu\text{m}$ Square with Ports IVIV for $B = -1\ \text{T}$	25
18	Potential and Current for a $10\ \mu\text{m}$ Square with Ports IVIV for $B = 0\ \text{T}$	26
19	Potential and Current for a $10\ \mu\text{m}$ Square with Ports IVIV for $B = 1\ \text{T}$	26
20	Resistance Versus Magnetic Field for a $10\ \mu\ \text{m}$ Square with Ports IVIV	27
21	Magnetoresistance Versus Magnetic Field for a $10\ \mu\text{m}$ Square with Ports IVIV	27
22	A schematic for a $10\ \mu\text{m}$ Square with Ports IVVI.....	28
23	Potential and Current for a $10\ \mu\text{m}$ Square with Ports IVVI for $B = -1\ \text{T}$	28
24	Potential and Current for a $10\ \mu\text{m}$ Square with Ports IVVI for $B = 0\ \text{T}$	29
25	Potential and Current for a $10\ \mu\text{m}$ Square with Ports IVVI for $B = 1\ \text{T}$	29
26	Resistance Versus Magnetic Field for a $10\ \mu\text{m}$ Square with Ports IVVI	30
27	Magnetoresistance Versus Magnetic Field for a $10\ \mu\text{m}$ Square with Ports IVVI	31
28	A schematic for a $300\ \text{nm}$ Square with Centered Ports	32

29	Potential and Current for a 300 nm Square with Centered Ports for $B = -1$ T	32
30	Potential and Current for a 300 nm Square with Centered Ports for $B = 0$ T .	33
31	Potential and Current for a 300 nm Square with Centered Ports for $B = 1$ T .	33
32	Resistance Versus Magnetic Field for a 300 nm Square with Centered Ports . .	34
33	Magnetoresistance Versus Magnetic Field for a 300 nm Square with Centered Ports	35
34	A schematic for a 1 μ m Circle with Equally Spaced Contacts	36
35	Resistance Versus Magnetic Field for a 1 μ m circle	36
36	Magnetoresistance Versus Magnetic Field for a 1 μ m circle	37
37	A schematic for a 10 μ m Square with Two Metal Regions and Current Ports along x	38
38	A schematic for a 10 μ m Square with Two Metal Regions and Current Ports along y	38
39	Potential and Current for a 10 μ m Square with Centered Ports along x and 2 metal regions for $B = -1$ T	39
40	Potential and Current for a 10 μ m Square with Centered Ports along x and 2 metal regions for $B = 0$ T	39
41	Potential and Current for a 10 μ m Square with Centered Ports along x and 2 metal regions for $B = 1$ T	40
42	Magnetoresistance Versus Magnetic Field for a 10 μ m Square with 2 Metal Regions and Ports Centered Along x	40
43	Potential and Current for a 10 μ m Square with Centered Ports along y and 2 metal regions for $B = -1$ T	41
44	Potential and Current for a 10 μ m Square with Centered Ports along y and 2 metal regions for $B = 0$ T	41
45	Potential and Current for a 10 μ m Square with Centered Ports along y and 2 metal regions for $B = 1$ T	42
46	Magnetoresistance Versus Magnetic Field for a 10 μ m Square with 2 Metal Regions and Ports Centered Along y	42
47	A Schematic for a 10 μ m Cube with \vec{B} Along y and z (Case 1)	43
48	A Schematic for a 10 μ m Cube with \vec{B} Along z Only (Case 2)	43
49	Potential Plot for the Cube (Case 1) with $x = 0$ μ m for $B = 0$ T	44

50	Potential Plot for the Cube (case 1) with $x = 5 \mu\text{m}$ for $B = 0 \text{ T}$	44
51	Potential Plot for the Cube (Case 1) with $x = 10 \mu\text{m}$ for $B = 0 \text{ T}$	45
52	Potential Plot for the Cube (Case 1) with $x = 0 \mu\text{m}$ for $B = -1 \text{ T}$	45
53	Potential Plot for the Cube (Case 1) with $x = 5 \mu\text{m}$ for $B = -1 \text{ T}$	46
54	Potential Plot for the Cube (Case 1) with $x = 10 \mu\text{m}$ for $B = -1 \text{ T}$	46
55	Current Plot for the Cube (Case 1) for $B = 0 \text{ T}$	47
56	Current Plot for the Cube (Case 1) for $B = -1 \text{ T}$	47
57	Potential Plot for the Cube (Case 2) with $x = 0 \mu\text{m}$ for $B = 0 \text{ T}$	48
58	Potential Plot for the Cube (Case 2) with $x = 5 \mu\text{m}$ for $B = 0 \text{ T}$	48
59	Potential Plot for the Cube (Case 2) with $x = 10 \mu\text{m}$ for $B = 0 \text{ T}$	49
60	Potential Plot for the Cube (Case 2) with $x = 0 \mu\text{m}$ for $B = 1 \text{ T}$	49
61	Potential Plot for the Cube (Case 2) with $x = 5 \mu\text{m}$ for $B = 1 \text{ T}$	50
62	Potential Plot for the Cube (Case 2) with $x = 10 \mu\text{m}$ for $B = 1 \text{ T}$	50
63	Current Plot for the Cube (Case 2) for $B = 0 \text{ T}$	51
64	Current Plot for the Cube (Case 2) for $B = 1 \text{ T}$	51

I. INTRODUCTION

Magnetic materials and artificially layered metals exhibit giant magnetoresistance (GMR) and manganite perovskites show colossal magnetoresistance (CMR), their nomenclature suggesting unusually high magnetoresistance (MR) of the structures in externally applied magnetic fields. However, patterned nonmagnetic metal-InSb shows a much larger geometrically enhanced MR even at room temperature and with no magnetic materials.¹ This effect is so large that it has been called extraordinary magnetoresistance (EMR).^{2,3} This phenomenon is a member of a class of effects labeled by EXX (piezoconductance (EPC),⁴⁻⁷ optoconductance (EOC),⁸⁻¹⁰ and electroconductance (EEC)¹¹ being the other effects) observed in metal-semiconductor hybrid structures that show a remarkably high response to external perturbations. The magnetoresistance (MR) is defined as $MR = [R(H) - R(0)]/R(0)$, where $R(H)$ is the resistance at finite field H . Because they are nonmagnetic and work at room temperature, EMR devices can be used in applications where typical magnetic sensors are not suitable. Furthermore, their performance continues to be impressive down to the nanoscale. Unlike traditional magnetic recording sensor technologies, such as GMR and tunnel magnetoresistive (TMR) sensors, where device resistance is determined by spin dependent scattering, in EMR structures the magnetoresistance is modulated by utilizing the Lorentz force to steer an electron current away from the high conduction metallic regions. The carrier velocity has a non-zero Hall angle with respect to the electric field which continues to be directed normal to the essentially equipotential metal-semiconductor interface.

The experiments were initially performed on a composite van der Pauw disk of a semiconductor matrix with an embedded metallic circular inhomogeneity that was concentric with the semiconductor disk. A finite element approach to modeling was developed earlier by us,¹² and the calculated MR based on a diffusive model for the current-electric field relation ($\mathbf{J} = \boldsymbol{\sigma} \cdot \mathbf{E}$), provides a striking agreement with experimental results for the MR for the circular geometry.¹² A similar enhancement has been reported¹ for a rectangular semiconductor wafer with a metallic shunt on one side. The rectangular geometry with four contacts can be shown to be derivable from the circular geometry by a conformal mapping,¹³ and the rectangular geometry is the desired form from device fabrication considerations as for most semiconductor devices. So it is natural to consider variations of the rectangular embedding of metal in a semiconductor as the most convenient for experimental fabrication.

An application of our original shunt geometry is to use the EMR device as a read-head for reading out data from magnetic storage hard-disks.^{3,14-16} The planar geometry of thin wafers results in a device that is sensitive to magnetic fields perpendicular to the plane of the wafer rather than the more typical in-plane field sensitivity demonstrated by GMR and TMR. This characteristic enables consideration of integrating EMR into unique planar recording head configurations. Commercial efforts in this direction are already under way. Further elaborations on the geometric enhancement of MR are discussed in Ref. 17.

In this article, we wish to consider the promise of very high MR in the metal-semiconductor structures by designing new schemes that could substantially enhance the EMR effect, and by modeling realistic two-dimensional (2D) and 3D structures that could be fabricated using Au/InSb. Here we develop the theory for such analysis, and demonstrate that geometrical enhancement of MR can be increased considerably with no more effort than used in making devices employed in earlier experiments with simple shunt devices. We provide estimates for devices of mesoscopic and nanoscopic dimensions, keeping in mind the recent technological advances in material fabrication today.

The theoretical development, presented in Section II, unlike earlier treatments discusses the use of high accuracy finite elements with \mathcal{C}_1 - or derivative - continuity. The use of Hermite interpolation polynomials¹⁸ for this purpose allows us to implement the derivative boundary conditions at interfaces very much more accurately than with Lagrange interpolation polynomials. All potential function and current boundary conditions can be explicitly implemented with Hermite interpolation polynomials, given their \mathcal{C}_1 degrees of freedom. Results of our analysis are given in Section III followed by concluding remarks in Section IV.

II. THEORETICAL CONSIDERATIONS

In the presence of a magnetic field, the magneto-conductivity is given in terms of $\vec{\beta} = \mu \vec{H}$ where μ is the carrier mobility and H is the magnetic field. In 3D, we have

$$\sigma = \frac{\sigma_0}{1 + \beta_x^2 + \beta_y^2 + \beta_z^2} \begin{pmatrix} (1 + \beta_x^2) & (-\beta_z + \beta_y\beta_x) & (\beta_y + \beta_z\beta_x) \\ (\beta_z + \beta_y\beta_x) & (1 + \beta_y^2) & (-\beta_x + \beta_y\beta_z) \\ (-\beta_y + \beta_z\beta_x) & (\beta_x + \beta_y\beta_z) & (1 + \beta_z^2) \end{pmatrix} \quad (1)$$

which reduces in 2D, with $\vec{H} = \hat{z}H$ and $\beta_z = \mu H$, to

$$\boldsymbol{\sigma} = \frac{\sigma_0}{1 + \beta_z^2} \begin{pmatrix} 1 & -\beta_z \\ \beta_z & 1 \end{pmatrix} \quad (2)$$

with only the x, y -components for the conductivity tensor. Here the intrinsic conductivity σ_0 is the conductivity in the absence of a magnetic field.

A. The Action Integral

In Refs. 12 and 15, we showed that a finite element approach^{18,19} to the calculation of the MR in simple 2D structures provides remarkable congruence with experimental results. Only linear interpolation polynomials were used in the calculations. Here we display the details of the theoretical development of the calculations for more complex geometries in 2D, keeping in mind that we will be investigating examples from 2D as well as 3D. We will also employ \mathcal{C}_1 -continuous functions which provide significant advantages in terms of accuracy, and also in terms of explicitly applying current continuity conditions at internal metal-semiconductor interfaces and derivative boundary conditions along the periphery.

In the present case of steady-state conditions the equation of continuity leads to

$$\nabla \cdot \mathbf{J} = 0 = \nabla \cdot (\boldsymbol{\sigma} \mathbf{E}), \quad (3)$$

or equivalently,

$$-\nabla \cdot \boldsymbol{\sigma} \cdot \nabla \phi(\mathbf{r}) = 0, \quad (4)$$

where the electric field \mathbf{E} is expressed in terms of a scalar potential ϕ . The use of variational methods provides fast, stable convergence in the calculations and we cast the problem using the principle of stationary action. The action integral from which this equation is derivable for Dirichlet boundary conditions is

$$A_0 = \int_0^T dt \sum_{\alpha} \left[\int_{\Omega_{\alpha}} d\mathbf{r} \frac{1}{2} \left(\partial_i \phi(\mathbf{r}) \sigma_{ij}^{(\alpha)} \partial_j \phi(\mathbf{r}) \right) \right]. \quad (5)$$

The sum over α is to account for the actions in different regions Ω_{α} with their different conductivities. In the steady state under consideration here, the integration over time is

trivial. Let us consider a typical 4-probe system for measuring the MR in the structure (see Fig. 3). The presence of current boundary conditions at two of the ports, corresponding to derivative boundary conditions, requires a modification of the above action in order to ensure that the equation of motion can be derived consistently. We suppose that the steady current comes in at port P_1 , say, and leaves the structure at port P_2 . The additional terms that are needed can be identified by analytically attempting to obtain the equation of motion as follows. A variation of A_0 with respect to the potential function ϕ together with the usual integration by parts leads to

$$\delta_\phi(A_0/T) = 0 = \sum_\alpha \left[\int_{S_\alpha} d\mathbf{r} \delta\phi \left(-\nabla \cdot \boldsymbol{\sigma}^{(\alpha)} \cdot \nabla \phi(\mathbf{r}) \right) \right] + \sum_\beta \int_{\Gamma_\beta} dl \delta\phi \hat{n} \cdot \left(\boldsymbol{\sigma}^{(\beta)} \cdot \nabla \phi(\mathbf{r}) \right). \quad (6)$$

Here β corresponds to the various contours at the peripheries of the various regions and \hat{n} is the normal to the counter-clockwise boundary paths in 2D. It is clear that if we had Dirichlet boundary conditions specifying the potential everywhere along the external periphery, the second term in Eq. (6), which we refer to as the surface term in both 2D and 3D, would vanish since ϕ is then fixed on the boundary. We note that (i) the requirement of continuity of the current across the metal-semiconductor interface always ensures that the integrals along Γ_2 and Γ_3 cancel (see Fig. 3). We also note that (ii) The potential at, say, P_3 is set to zero to give a reference potential, hence the boundary integral across Δ_3 is zero ($\delta\phi$ is zero there since ϕ is zero there and is therefore fixed in value). (iii) Our boundary conditions are not of the Dirichlet type along the outer periphery at the current ports so that the portions of Γ_1 corresponding to $\Delta_{1,2}$ require special consideration. Using the relation $\mathbf{J} = -\boldsymbol{\sigma} \nabla \phi(\mathbf{r})$, we can identify the integrand of the surface term in square brackets in terms of the current there. Since no current comes in or escapes along Γ_1 except at the ports P_1 and P_2 , we can set the contour integral to zero everywhere except over Δ_1 and Δ_2 . The potential at port P_4 is determined by the solution there as discussed below. (iv) The two surface terms at $\Delta_{1,2}$ are such that $\delta\phi$ are arbitrary there, and $-\boldsymbol{\sigma} \nabla \phi \cdot \hat{n}$ is nonzero. Since these two surface terms cannot be set to zero the equation of motion, Eq. (4), does not hold. This is remedied by adding two additional terms to the action that ensure that these surface terms are cancelled

out.^{12,20} Writing the new action, we have

$$A/T = \sum_{\alpha} \int d\mathbf{r} \frac{1}{2} \left(\partial_i \phi(\mathbf{r}) \sigma_{ij}^{(\alpha)} \partial_j \phi(\mathbf{r}) \right) - \int_{\Delta_1} d\ell \phi(x, y)|_{\Delta_1} J_{\text{in}} + \int_{\Delta_2} d\ell \phi(x, y)|_{\Delta_2} J_{\text{out}}, \quad (7)$$

with the current boundary conditions incorporated into the action. We note that while the current I_{in} must equal I_{out} , the width of the contacts $\Delta_{1,2}$ and the thickness of the semiconductor wafer determine the current densities $J_{1,2}$. The same considerations apply to a 3D geometry with the extension of the above expressions to metallic inclusions in a semiconductor volume.

We now evaluate the action directly by discretization of the physical space using the finite element method (FEM), as discussed in the following.

B. The Finite Element Method with \mathcal{C}_1 -continuous Elements

In the finite element method, the physical domain is discretized into elements. In each of the elements the variational principle holds. The potential function is represented as a polynomial multiplied by coefficients representing the value of the potential at special points in the element called nodes. On integrating out the spatial dependence, the action reduces to a bilinear expression in the as-yet unknown interpolation coefficients, which are known as the nodal variables. The principle of stationary action is invoked by varying A/T with respect to the nodal variables, which then leads to a system of simultaneous equations that represent the discretized equation of motion.¹⁸

The simultaneous equations are solved to obtain the potentials at the nodes and the potential everywhere is reconstructed using the original interpolation polynomial in each element. This allows us to also obtain the current density in great detail, and we then determine the MR for a range of values of the magnetic field H .

Since the predominant practical choice of device geometry is rectangular, we consider finite elements of the same shape. In 2D, consider a standard square element with nodes at $\xi = \pm 1, \eta = \pm 1$. A given rectangular element can be linearly mapped into the standard element, so that the interpolation polynomials can be defined on the standard element for convenience. Each of the four nodes at the four corners of the element are associated with the values of the potential and its derivatives $\{\phi^{(in)}, \phi_{,\xi}^{(in)'}, \phi_{,\eta}^{(in)'}, \phi_{,\xi\eta}^{(in)''}\}$, where $in = 1, \dots, 4$,

for the four nodes. Thus there are 4 degrees of freedom (DoF) at each of the four nodes of the element. This is shown in Fig. 1 The corresponding \mathcal{C}_1 -continuous (Hermite) interpolation polynomials are given in Ref.18. For Hermite interpolation polynomials $N_\nu(x, y)$, or shape functions as the interpolation polynomials are called in finite element analysis, we represent the potential function over a given element as

$$\phi(x, y) = \sum_{\nu} \phi_{\nu} N_{\nu}(x, y), \quad (8)$$

with the sum running over the full set of 16 DoF for the element. The action is calculated over each element and the spatial variables are integrated out. The resulting expression is bilinear in the nodal variables and can be cast in a matrix form. The element matrices are then overlaid to account for the continuity of the solution over the individual materials of the composite, keeping account of the interface boundary conditions. In summary, the discretized action obtained from Eq.(7) can be written as

$$A/T \doteq \frac{1}{2} \phi_{\alpha} M_{\alpha\beta} \phi_{\beta} - \phi_{\alpha} [\delta_{\alpha\tau_1} R_{\tau_1}^{\text{in}}] J_{\text{in}} + \phi_{\alpha} [\delta_{\alpha\tau_2} R_{\tau_2}^{\text{out}}] J_{\text{out}} \quad (9)$$

where the surface integrals in Eq.(7) are designated by the nodal values multiplied by integration of shape functions only over the current ports in the last two terms.

C. Boundary Conditions for Hermite Elements

The boundary conditions for the potential and its derivatives are readily implemented within the finite element scheme.

- (a) The continuity of the potential across the metal-semiconductor interface can be enforced by setting the nodal values

$$\phi_{in}^I = \phi_{in}^{II}. \quad (10)$$

The continuity of the normal current across the interface requires

$$\hat{n}_i \sigma_{ij}^{(I)} \partial_j \phi^{(I)}(x, y) = \hat{n}_i \sigma_{ij}^{(II)} \partial_j \phi^{(II)}(x, y),$$

so that at each of the nodes common to the paths $\Gamma_{2,3}$ where, for example, $\hat{n}_\mu = \hat{y}$ we use the relation

$$\begin{pmatrix} 1 & 0 & 0 & 0 \\ 0 & 1 & 0 & 0 \\ 0 & \sigma_{yx}^{(I)} & \sigma_{yy}^{(I)} & o \\ 0 & 0 & 0 & 1 \end{pmatrix} \begin{pmatrix} \phi^{(I)} \\ \phi_x^{(I)'} \\ \phi_y^{(I)'} \\ \phi_{xy}^{(I)''} \end{pmatrix} = \begin{pmatrix} 1 & 0 & 0 & 0 \\ 0 & 1 & 0 & 0 \\ 0 & \sigma_{yx}^{(II)} & \sigma_{yy}^{(II)} & o \\ 0 & 0 & 0 & 1 \end{pmatrix} \begin{pmatrix} \phi^{(II)} \\ \phi_x^{(II)'} \\ \phi_y^{(II)'} \\ \phi_{xy}^{(II)''} \end{pmatrix}; \quad (11)$$

a similar relation holds for the current continuity of J_x across the interfaces with constant y . Thus the first-derivative degrees of freedom are reduced appropriately to enforce the current continuity.

- (b) No current enters or leaves the device on the outer boundary Γ_2 other than at the current ports. We therefore require that

$$J_n = \sigma_{nx} \frac{\partial \phi}{\partial x} + \sigma_{ny} \frac{\partial \phi}{\partial y} = 0, \quad (12)$$

except at the current ports. This again allows us to reduce the nodal derivative degrees of freedom by one at every node on the external boundary. The variables $\phi^{(in)}$ and $\phi_{,xy}^{(in)''}$ on the boundary are not preassigned any values since they have no conditions on them.

- (c) At the voltage port P_3 , the potential at the nodes is set to zero, while the normal current is eliminated as in the boundary condition (b) above. At the voltage port P_4 , the potential is not determined, but the normal current is again eliminated since no current leaves the system at P_4 . In order to make the contact an equipotential we ensure that the potential variables ϕ^{in} are equated to one another as follows.

Suppose there are only two nodes N_1 and N_2 on P_4 , where $N_{1,2}$ refer to node numbers associated with a global node numbering for the entire structure. The discretized action leads to the matrix $M_{\alpha\beta}$ as in Eq. (7). The effect of equating the potentials $\phi_{N_1} = \phi_{N_2}$ is to add the row and column corresponding to N_1 onto the row and column for N_2 . After the transfer, the row and column of index N_1 is then zeroed out, and the matrix entry (N_1, N_1) is set to 1 while matrix entry (N_1, N_2) is set to -1 . This procedure is illustrated in Fig. 2.

As for the other degrees of freedom for these two ports, we treat them the same as the outer boundary since we do not want current going in or out. Therefore $\phi'_{,x}$ and $\phi'_{,y}$ follow the condition given in (a) above, and $\phi''_{,xy}$ is left floating.

The overlay of the calculations for the element matrices, consistent with the above element and interface boundary conditions, leads to the discretized action given by a global matrix M together with vectors representing the surface terms at the current ports. We have

$$A/T \doteq \frac{1}{2} \phi_{\alpha} M_{\alpha\beta} \phi_{\beta} - \phi_{\alpha} [\delta_{\alpha\tau_1} R_{\tau_1}^{\text{in}}] J_{\text{in}} + \phi_{\alpha} [\delta_{\alpha\tau_2} R_{\tau_2}^{\text{out}}] J_{\text{out}} \quad (13)$$

with the surface integral evaluated explicitly using the shape functions mentioned earlier. The nodal values for the potential over the entire domain are labeled by ϕ_{α} , and their values at the current ports are limited to the nodes labeled by τ_1 and τ_2 that are located there. The principle of stationary action is implemented by varying the above discretized action with respect to ϕ_{α} and thereby obtaining the matrix equation that represents the original differential equation. We solve the matrix equation

$$M_{\alpha\beta} \phi_{\beta} = [\delta_{\alpha\tau_1} R_{\tau_1}^{\text{in}}] J_{\text{in}} - [\delta_{\alpha\tau_2} R_{\tau_2}^{\text{out}}] J_{\text{out}} \quad (14)$$

for the potential at the nodes over the entire domain.

III. THE MAGNETORESISTANCE

A. A Rectangular Metallic Region Embedded in a Semiconductor

As shown in Fig. 3, the first case considered is a rectangular semiconductor with a single embedded square metal region. The contacts can be placed anywhere on the edges of the device, and the overall size as well as the size and position of the metal region can vary as well. First, a $10\ \mu\text{m}$ semiconductor square is considered for various dimensions of the embedded metal square, as well as a $300\ \text{nm}$ semiconductor square to demonstrate that the EMR effect is scalable. This is followed with discussion of more complicated geometries.

1. $10\ \mu\text{m}$, *Centered Ports*

For a $10\ \mu\text{m}$ square, we first consider the ports that are centered on all sides as shown in Fig. 4. For a $5\ \mu\text{m}$ metal region, Fig. 5, Fig. 6, and Fig. 7 all show a plot of the potential and the current for $B = -1\ \text{T}$, $B = 0\ \text{T}$, and $B = 1\ \text{T}$, respectively. Note that the current is represented by vectors which show the direction, and by a color gradient which represents the magnitude. As expected we see that for zero field the current is normal to the surface of the metal, and for higher fields the current curves around the metal and concentrates in the semiconductor region, causing a change in resistance. Fig. 8 shows a plot of the resistance obtained from this configuration versus the applied magnetic field for various widths of the inner metal square region, where for each case the inner square is centered. Fig. 9 shows a plot of the magnetoresistance versus the applied magnetic field. Note that this is a log-log plot and the dashed lines represent the negative portion of the magnetic field for each case. For an inner square width of $8\ \mu\text{m}$ for $B = 1\ \text{T}$ and $B = -1\ \text{T}$, we see an MR on the order of almost $10^7\%$.

2. $10\ \mu\text{m}$, *Diagonal Ports*

The next case considered is a $10\ \mu\text{m}$ square with diagonal ports as shown in Fig. 10. Once again for a $5\ \mu\text{m}$ metal region, Fig. 11, Fig. 12, and Fig. 13 all show a plot of the potential and the current for $B = -1\ \text{T}$, $B = 0\ \text{T}$, and $B = 1\ \text{T}$, respectively. Fig. 14 shows a plot of the resistance versus the applied magnetic field for various widths of the metal region. The result is very similar to what is obtained in the previous case for centered ports. However, a plot of the MR versus the magnetic field shows the differences, as seen in Fig. 15. In this case for a width of $8\ \mu\text{m}$ we see the greatest MR for $B = -1\ \text{T}$ is on the order of $10^6\%$.

3. $10\ \mu\text{m}$, *Ports IVIV*

Another contact configuration is shown in Fig. 16. In this case all four contacts are on one side of the semiconductor, and is alternating between current and potential. Fig. 17, Fig. 18, and Fig. 19 show the plots of the potential and current for B ranging from $-1\ \text{T}$ to $1\ \text{T}$. Fig. 20 shows the resistance versus the magnetic field which is much different than the previous two cases. In Fig. 21 a plot of the magnetoresistance versus the magnetic field

is shown. Once again we see a lower MR compared to the square with centered ports. For $a = 8 \mu\text{m}$ at $B = -1 \text{ T}$, there is a maximum MR on the order of $10^4\%$.

4. $10 \mu\text{m}$, Ports IVVI

Fig. 22 shows another configuration similar to the previous one with all ports on one side, but now with two of the ports swapped. Once again the potential and current for $B = -1, 0, 1 \text{ T}$ are shown in Fig. 23, Fig. 24, and Fig. 25, respectively. This time there is a drastic change in the resistance versus magnetic field plot, shown in Fig. 26. The plot of the magnetoresistance, shown in Fig. 27, has a similar maximum as the previous case for ports IVIV, but this time has a non monotonic behavior for positive values of the magnetic field.

5. 300 nm , Centered Ports

A 300 nm square with a square metallic region was also examined to show that the MR effect is scalable. The same input current was used. The schematic for this is shown in Fig. 28. The potential and current are shown in Fig. 29, Fig. 30, and Fig. 31. The resistance versus magnetic field is shown in Fig. 32. *The magnitude of the current, potential, and resistance have different magnitudes than for the $10 \mu\text{m}$ cases with centered ports, but the MR, shown in Fig. 33, is identical to that of the $10 \mu\text{m}$ square (previously shown in Fig. 9).* This shows that the MR is scale invariant.

B. Circular Metallic Region Embedded in a Semiconductor

A circular semiconductor with a circular metal region was also modeled in order to compare with previous results. The contacts on the circle were equally spaced as shown in Fig. 34. The plots of resistance and MR versus magnetic field are shown in Fig. 35 and Fig. 36, respectively. The maximum MR in this case for $B = \pm 1 \text{ T}$ is just over $10^5\%$ for an inner radius of $r = 0.7 \mu\text{m}$.

C. Multiple Metallic Regions Embedded in a 2D Semiconductor Wafer

Because of the flexibility of FEM we can easily add multiple metal regions to the semiconductor. Fig. 37 shows a $10\ \mu\text{m}$ semiconductor with two embedded metal regions. The length and width of these regions can be adjusted as well as the positions of the contacts. As in Fig. 37, the current ports are centered along x , where in Fig. 38 they are centered along y . We will examine both of these cases.

1. Multiple Regions with Current Ports along x

We first look at a $10\ \mu\text{m}$ square semiconductor with two embedded rectangular metal regions which has current ports centered along the x -axis. Fig. 39, Fig. 40, and Fig. 41 show plots of the current and potential for $B = 1, 0$, and $-1\ \text{T}$. In these plots, we are using metal regions of width $a = 2.5\ \mu\text{m}$, height $b = 5\ \mu\text{m}$, separated by a distance of $d = 2.5\ \mu\text{m}$. The magnetoresistance for this case, which we call case D, is shown in Fig. 42 along with three more examples, cases A, B and C. For case A, we have $a = 3.5\ \mu\text{m}$, $b = 8\ \mu\text{m}$, and $d = 1\ \mu\text{m}$. For cases B and C, we have $a = 3.25\ \mu\text{m}$, $b = 7\ \mu\text{m}$, $d = 0.5\ \mu\text{m}$, and $a = 3.9\ \mu\text{m}$, $b = 8\ \mu\text{m}$, $d = 0.2\ \mu\text{m}$, respectively. We see that case A gives us the highest magnetoresistance, just over 10^7 percent for $1\ \text{T}$, which is slightly better than what was obtained for the square metal region with centered ports for $1\ \text{T}$.

2. Multiple Regions with Current Ports along y

Next we look at a $10\ \mu\text{m}$ square semiconductor with two embedded rectangular metal regions which has current ports centered along the y -axis. Fig. 43, Fig. 44, and Fig. 45 show plots of the current and potential for $B = 1, 0$, and $-1\ \text{T}$ for case D mentioned in the previous section. Fig. 46 shows the magnetoresistance for cases A,B,C and D. In this case we get a maximum MR of less than 10^5 percent. So, in this case the ports centered on the x -axis is preferable.

D. Metallic Cube Embedded in a 3D Semiconductor Cube

Fig. 47 and Fig. 48 show two examples of a three-dimensional semiconductor cube. The results shown below all have an embedded metal region of $5\ \mu\text{m}$. In the first case, which we will call case 1, we have a magnetic field along both the y and z directions, with 2 contacts on the front face and 2 contacts on the back face. In case 2, we have a magnetic field only along z , with current contacts on the left and right faces and voltage contacts on the front and back. This case is analogous to the two-dimensional case where there is one square metal region with contacts centered on all sides.

First we will look at the results for case 1. Fig. 49, Fig. 50, and Fig. 51 show plots of the potential in the y - z plane for $B = 0\ \text{T}$ for various x coordinates ($x = 0, 5, 10\ \mu\text{m}$, respectively). The same is shown in Fig. 52, Fig. 53, and Fig. 54, but for $B = -1\ \text{T}$. Three dimensional vector field plots for the current are shown in Fig. 55 and Fig. 56 for $B = 0\ \text{T}$ and $B = -1\ \text{T}$.

For case 2, Fig. 57, Fig. 58, and Fig. 59 show the potential plots in the y - z plane for $B = 0\ \text{T}$ for various x coordinates ($x = 0, 5, 10\ \mu\text{m}$, respectively). The same is shown in Fig. 60, Fig. 61, and Fig. 62 but for but for $B = 1\ \text{T}$. Three dimensional vector field plots for the current are shown in Fig. 63 and Fig. 64 for $B = 0\ \text{T}$ and $B = 1\ \text{T}$.

For case 1, we see a maximum MR of 346% for a field of $-1\ \text{T}$ and 556% for a field of $1\ \text{T}$. However in case 2 we see a much larger MR, which is 27,356% for $-1\ \text{T}$ and 26,495% for $1\ \text{T}$. If we compare this to the two-dimensional case with ports centered on all sides and an inner square of $5\ \mu\text{m}$, the MR is on the same order of magnitude.

IV. CONCLUDING REMARKS

The use of the Finite Element Method produces highly accurate results, especially when using Hermite interpolation polynomials. FEM is advantageous because of the action integral formalism in which we can directly apply derivative boundary conditions for the current. It is also a very flexible method which transcends geometrical issues, so many possibilities for the geometry-dependent EMR calculations are feasible. Here we have shown that the Magnetoresistance effect can be optimized through changes in the geometry of the metal-semiconductor hybrid structure. The sensitivity of the device is based on intrinsic contributions from physical properties such as carrier mobility and energy band structure.¹⁷ However there is also a geometric contribution to the MR, which can play an even more important role. The geometric contribution which can include the size and shape of the metallic regions and the device as a whole, the number of metallic regions, and even the orientation of the current and potential ports.¹⁷ We can see this especially in the geometry of the square region with centered ports, where the highest MR is obtained for an inner metal width of $8 \mu\text{m}$ at fields of $B = \pm 1 \text{ T}$ and also for the $10 \mu\text{m}$ square with two metal regions and ports centered along x for 1 T. However, if we compare these two cases, when we have one metal region the greatest MR occurs when we have $64 \mu\text{m}^2$ of metal, and with multiple regions, this maximum occurs in case A when we have less metal - a total of $56 \mu\text{m}^2$. Even for lower values of the field, we see in most cases a very large MR which means that EMR read heads would be more sensitive than the currently used TMR read-heads. The three-dimensional model also shows some promising results for other applications. For the case (case 2) which is analogous to the 2D case with centered ports, we get an MR which is on the same order of magnitude for an inner metal width of $5 \mu\text{m}$.

ACKNOWLEDGMENTS

I would like to thank Cody Ahheng, Andrei Ilyashenko and Zehao Li for their help with some of the programming aspects of the work. I would also like to thank Paul Kassebaum for his help with visualization aspects. This work was supported by the National Science Foundation under grant number ECS-0725427. The computational resources at the Center for Computational NanoScience, WPI, and the use of finite element and sparse matrix analysis software from Quantum Semiconductor Algorithms, Inc., are gratefully acknowledged.

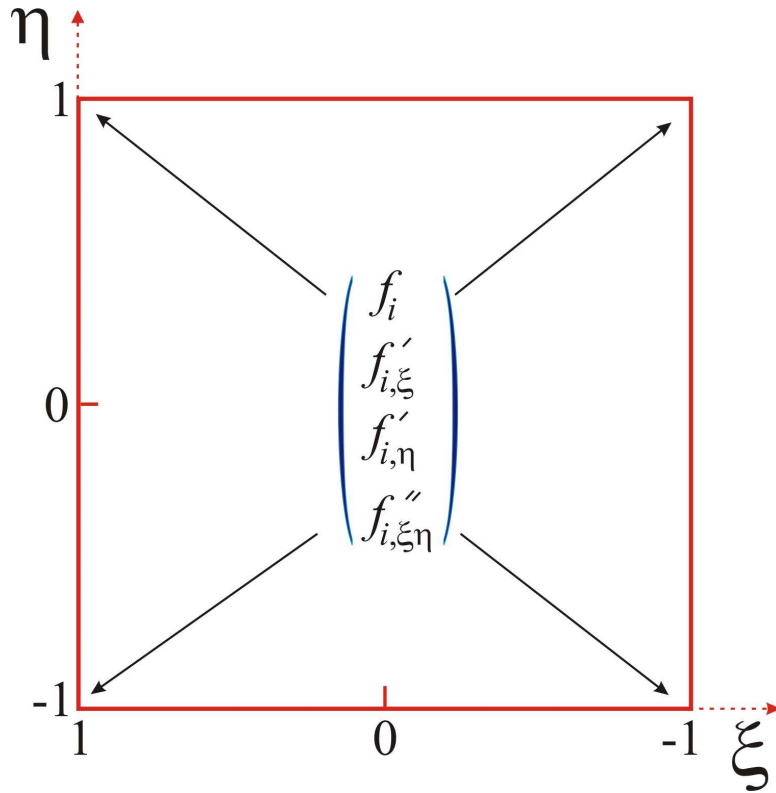


FIG. 1. A 2D reference finite element is shown with four degrees of freedom at nodes at the four corners corresponding to the value of the function, its first derivatives with respect to ξ, η and a second (cross) derivative. The polynomial interpolation within the element is performed using the values of the function and its derivatives at the nodes. See Ref. 18. This scheme is extended to 3D for a cube element.

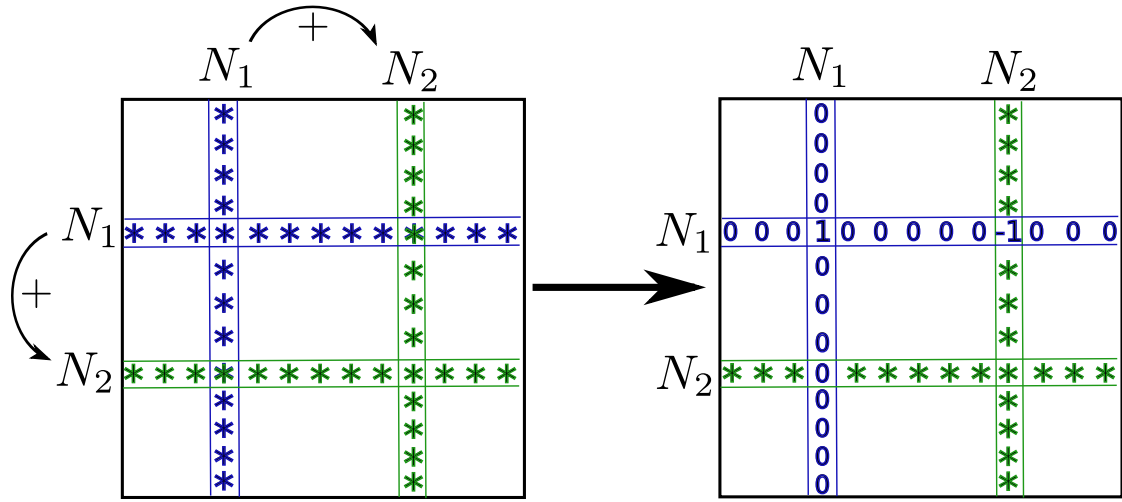


FIG. 2. The diagram illustrates the matrix manipulation for setting two nodal values to be the same. Matrix entries are rearranged as discussed in the text. This is done for all nodes on P_4 to make it an equipotential contact.

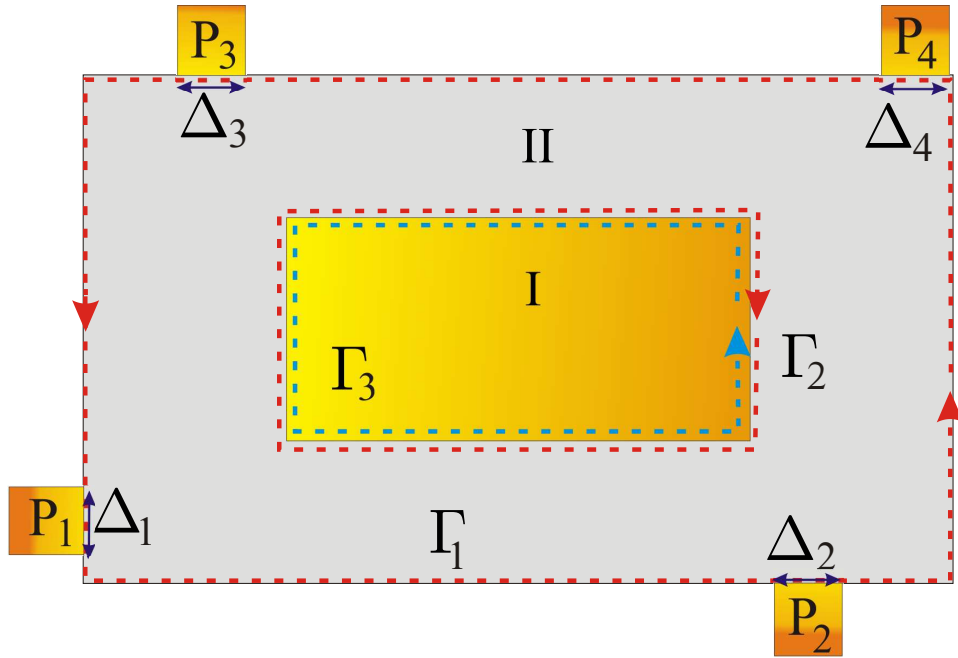


FIG. 3. A semiconductor wafer with a rectangular metallic inclusion is shown. Contacts P_1, \dots, P_4 correspond to two voltage probes P_3 and P_4 , with current I coming in at say P_1 and leaving the structure at P_2 . The current density entering the device is taken to be $I/(\Delta_1 t)$ where t is the thickness of the wafer and Δ_1 is the width of the contact. The metal and semiconductor are labeled by roman numerals.

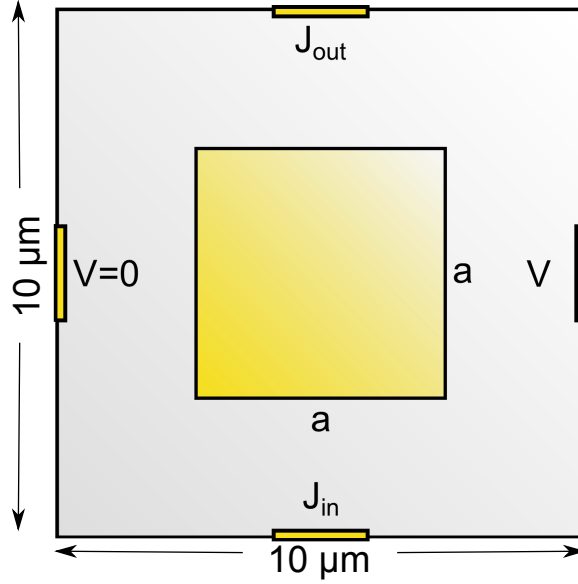


FIG. 4. A schematic for a $10\ \mu\text{m}$ square with ports centered on all sides.

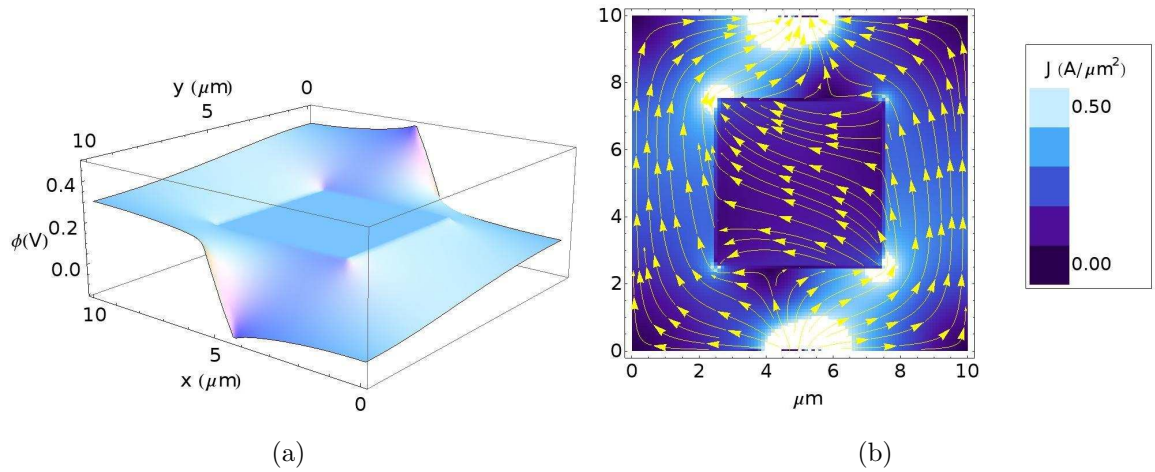


FIG. 5. The potential (a) and the plot of the current (b) for a $10\ \mu\text{m}$ square with centered ports with a $5\ \mu\text{m}$ metallic region and an applied field of $B = -1\ \text{T}$ are shown.

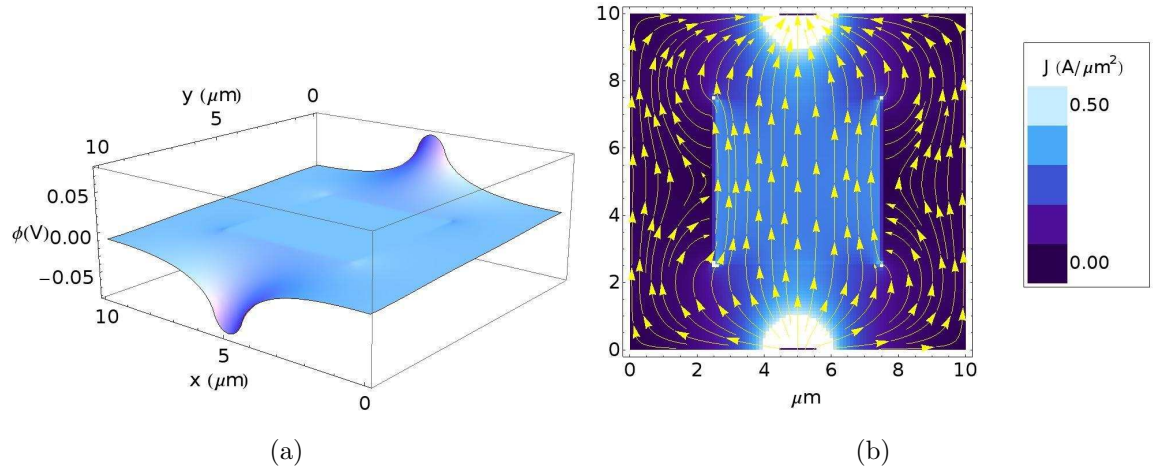


FIG. 6. The potential (a) and the plot of the current (b) for a $10\ \mu\text{m}$ square with centered ports with a $5\ \mu\text{m}$ metallic region and an applied field of $B = 0\ \text{T}$ are shown.

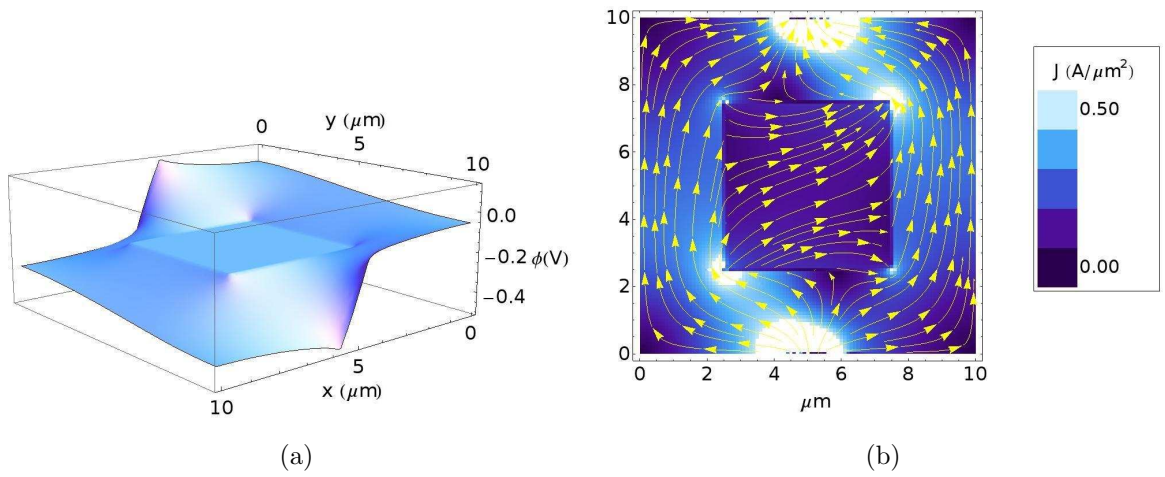


FIG. 7. The potential (a) and the plot of the current (b) for a $10\ \mu\text{m}$ square with centered ports with a $5\ \mu\text{m}$ metallic region and an applied field of $B = 1\ \text{T}$ are shown.

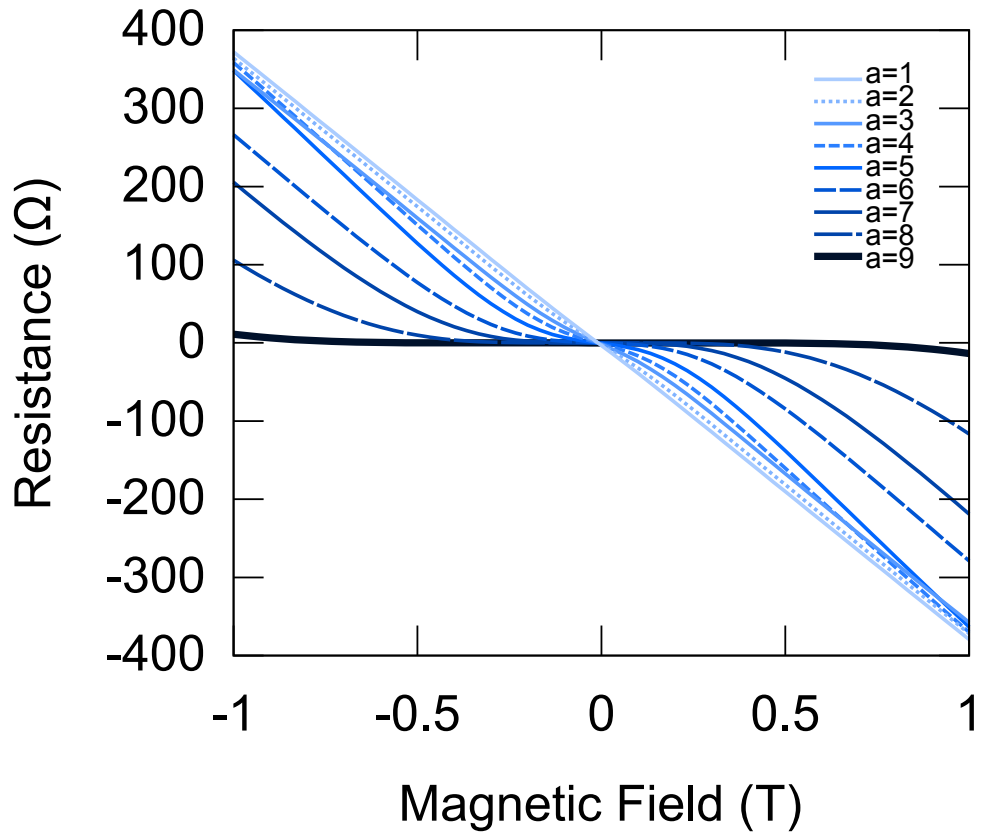


FIG. 8. Plot of the resistance versus the magnetic field for a $10\ \mu\text{m}$ square with ports centered on all sides.

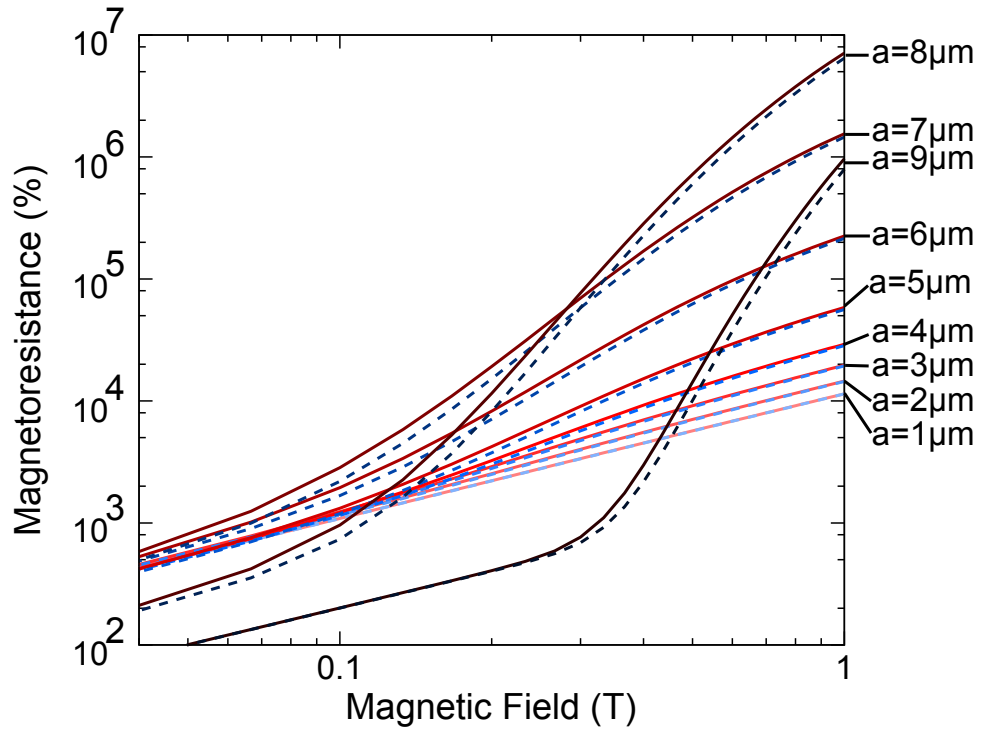


FIG. 9. Plots of the magnetoresistance versus the magnetic field for a $10\mu\text{m}$ square with ports centered on all sides for different square metallic regions of side a . The dashed lines represent the MR for negative values of the magnetic field.

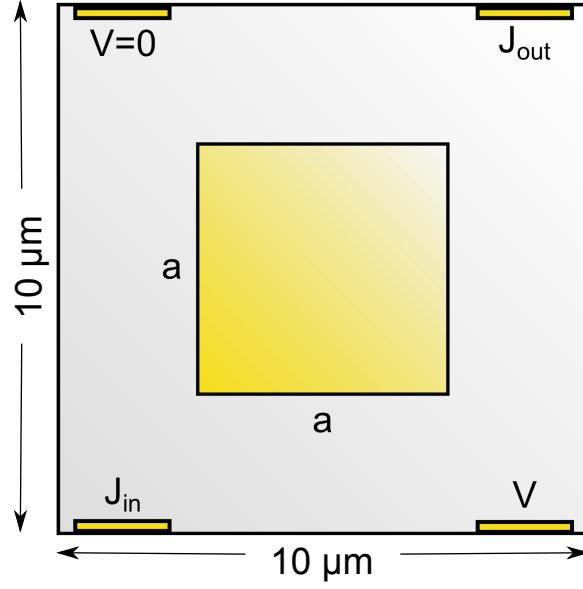


FIG. 10. A schematic for a $10\ \mu\text{m}$ square with diagonal ports.

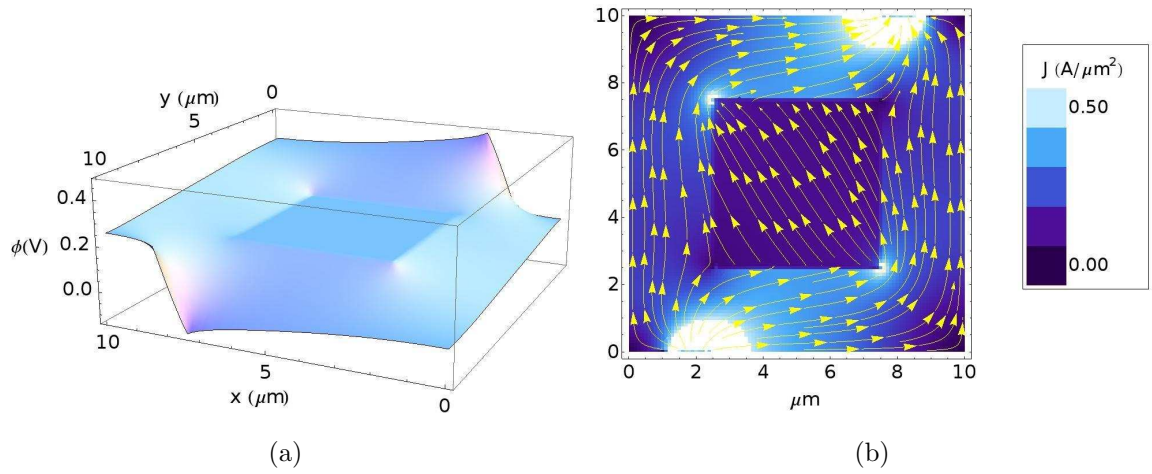


FIG. 11. The potential (a) and the plot of the current (b) for a $10\ \mu\text{m}$ square with diagonal ports with a $5\ \mu\text{m}$ metallic region and an applied field of $B = -1\ \text{T}$ is shown.

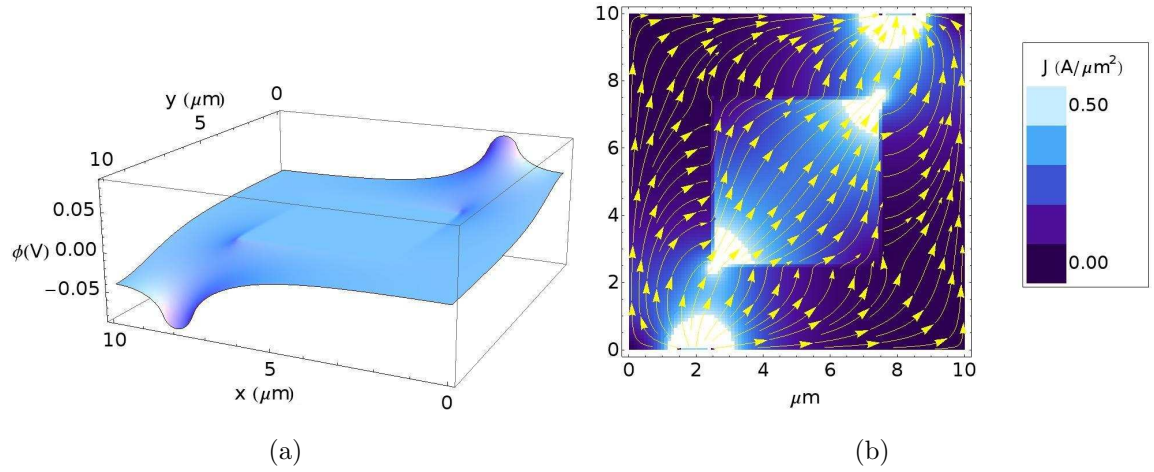


FIG. 12. The potential (a) and the plot of the current (b) for a $10\ \mu\text{m}$ square with diagonal ports with a $5\ \mu\text{m}$ metallic region and an applied field of $B = 0\ \text{T}$ is shown.

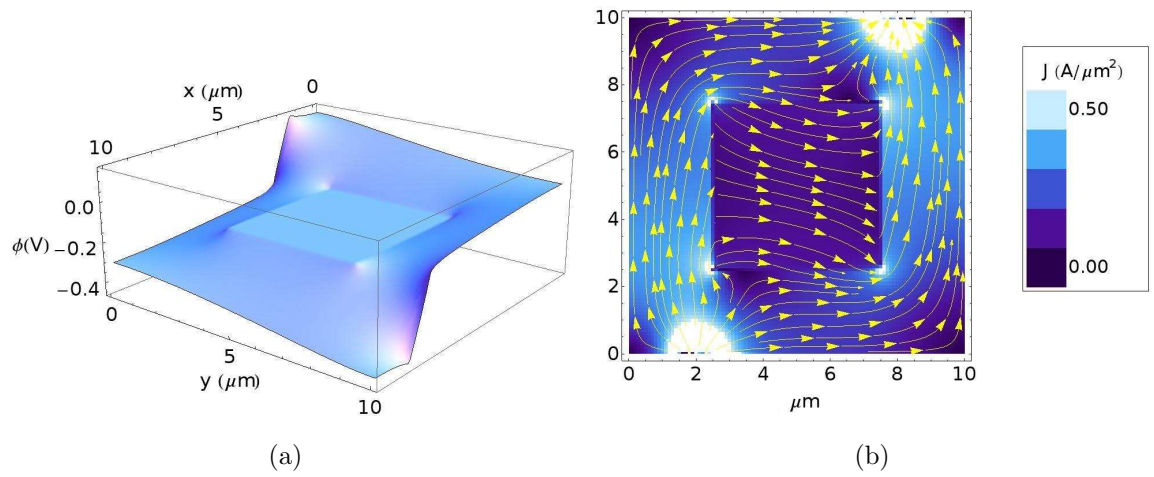


FIG. 13. The potential (a) and the plot of the current (b) for a $10\ \mu\text{m}$ square with diagonal ports with a $5\ \mu\text{m}$ metallic region and an applied field of $B = 1\ \text{T}$ is shown.

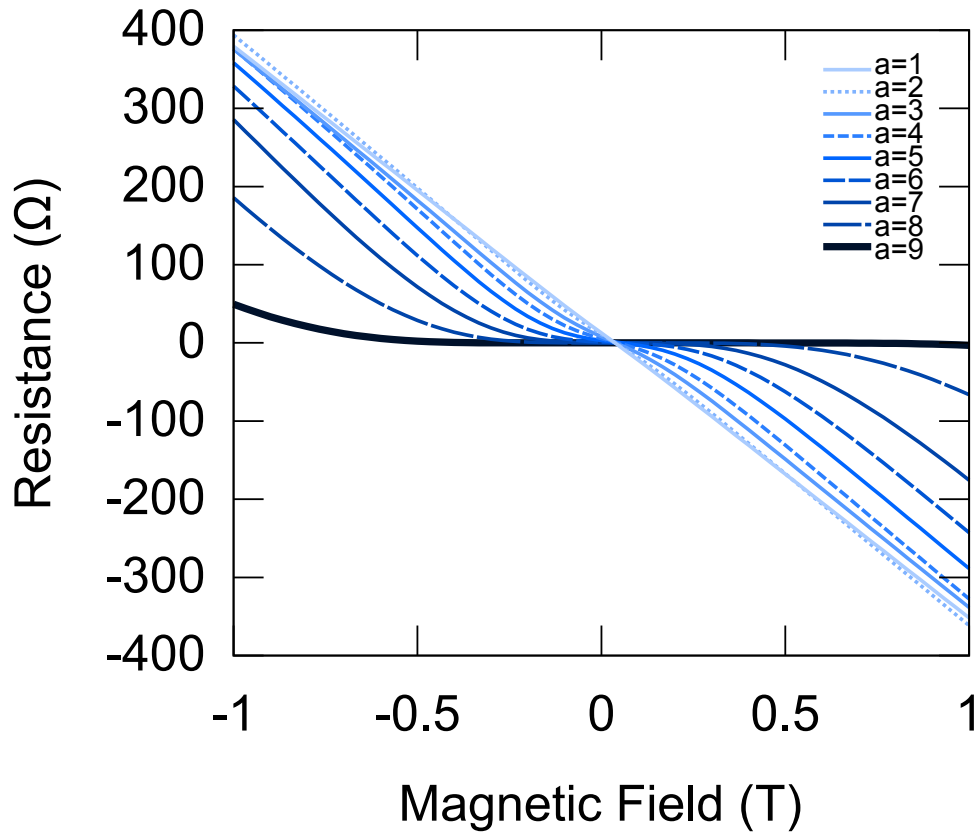


FIG. 14. Plots of the resistance versus the magnetic field for a $10 \mu\text{m}$ square with diagonal ports.

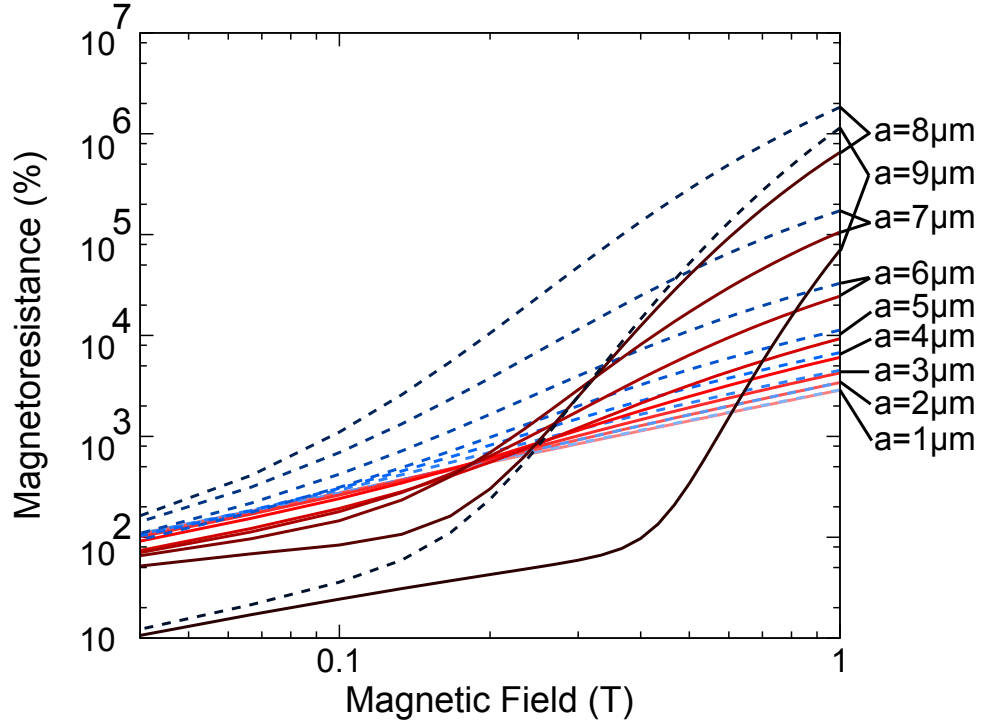


FIG. 15. Plots of the magnetoresistance versus the magnetic field for a $10 \mu\text{m}$ square with diagonal ports. The dashed lines represent the MR for negative values of the magnetic field.

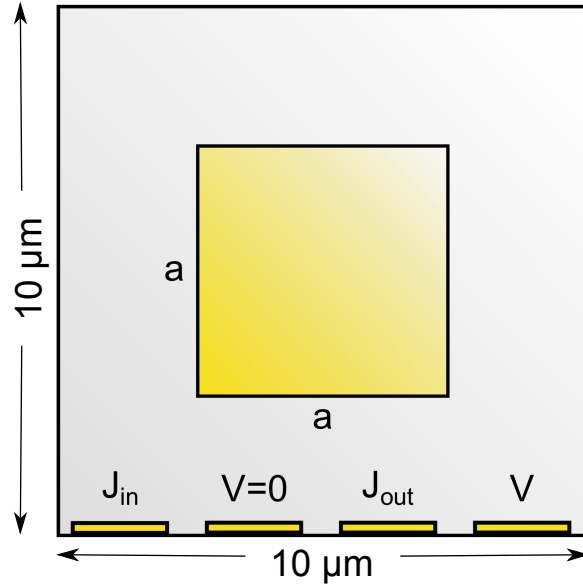


FIG. 16. A schematic for a $10\ \mu\text{m}$ square with ports IVIV.

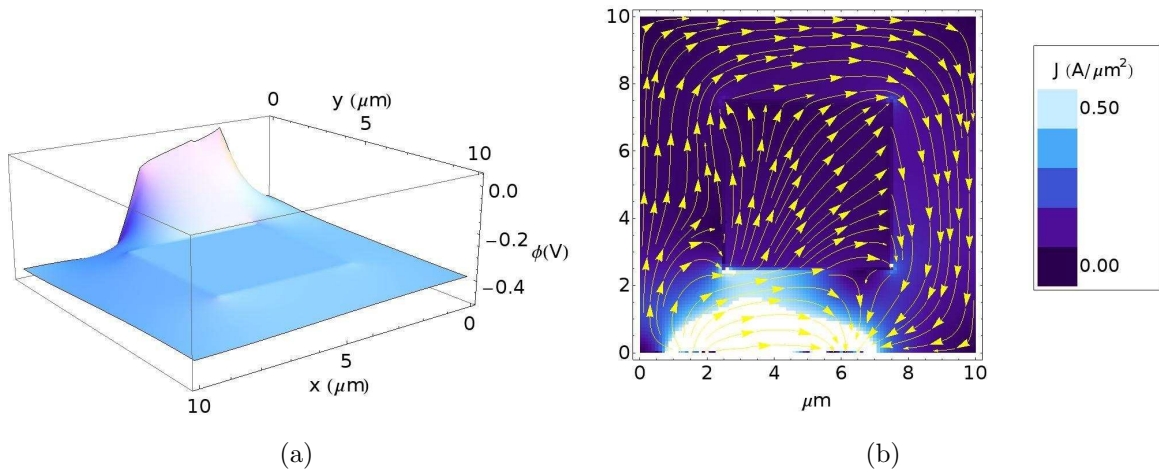


FIG. 17. The potential (a) and the plot of the current (b) for a $10\ \mu\text{m}$ square with ports IVIV with a $5\ \mu\text{m}$ metallic region and an applied field of $B = -1\ \text{T}$ is shown.

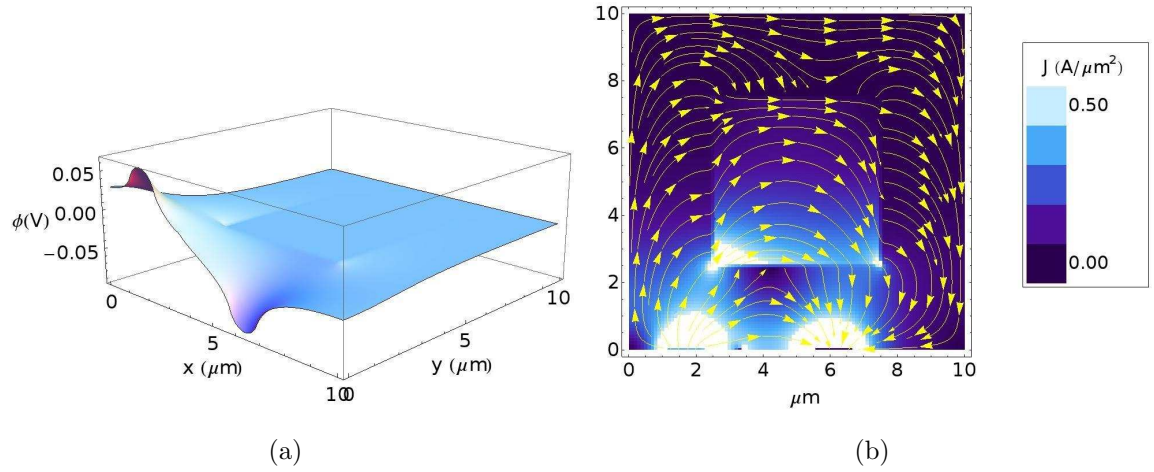


FIG. 18. The potential (a) and the plot of the current (b) for a $10\ \mu\text{m}$ square with ports IVIV with a $5\ \mu\text{m}$ metallic region and an applied field of $B = 0\ \text{T}$ is shown.

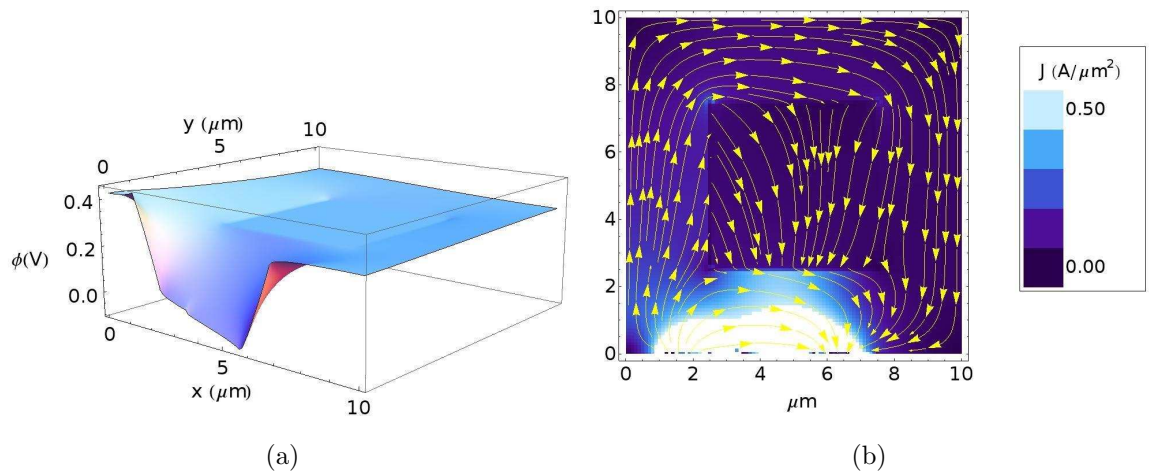


FIG. 19. The potential (a) and the plot of the current (b) for a $10\ \mu\text{m}$ square with ports IVIV with a $5\ \mu\text{m}$ metallic region and an applied field of $B = 1\ \text{T}$ is shown.

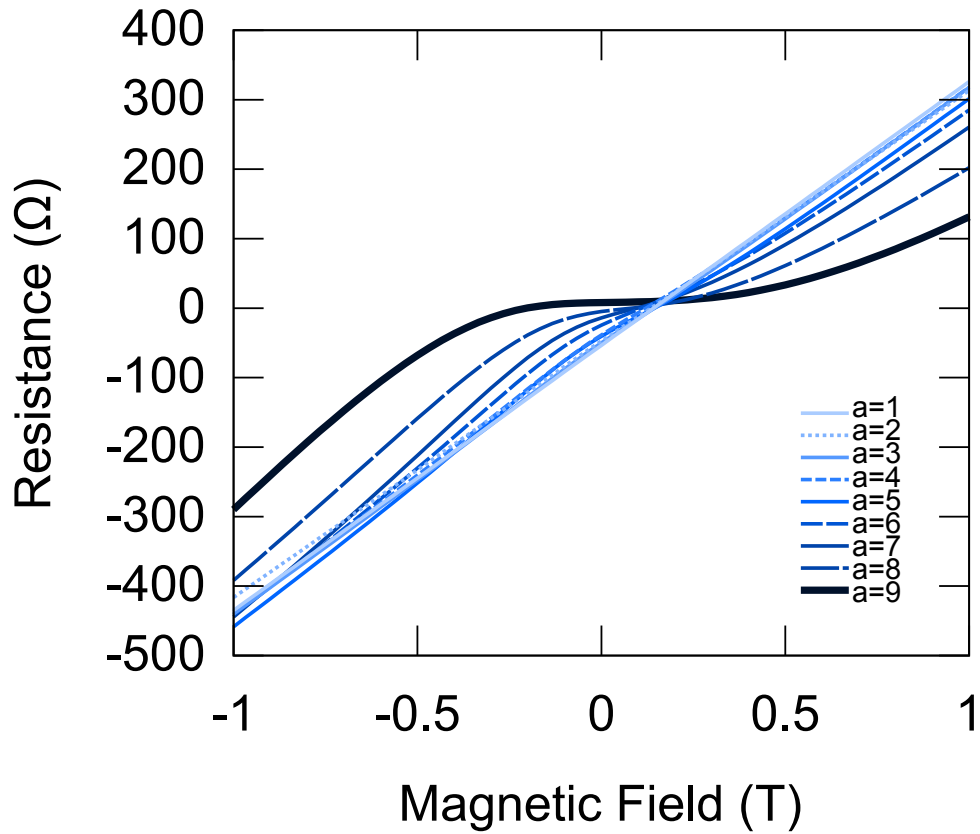


FIG. 20. Plots of the resistance versus the magnetic field for a $10 \mu\text{m}$ square with ports IVIV.

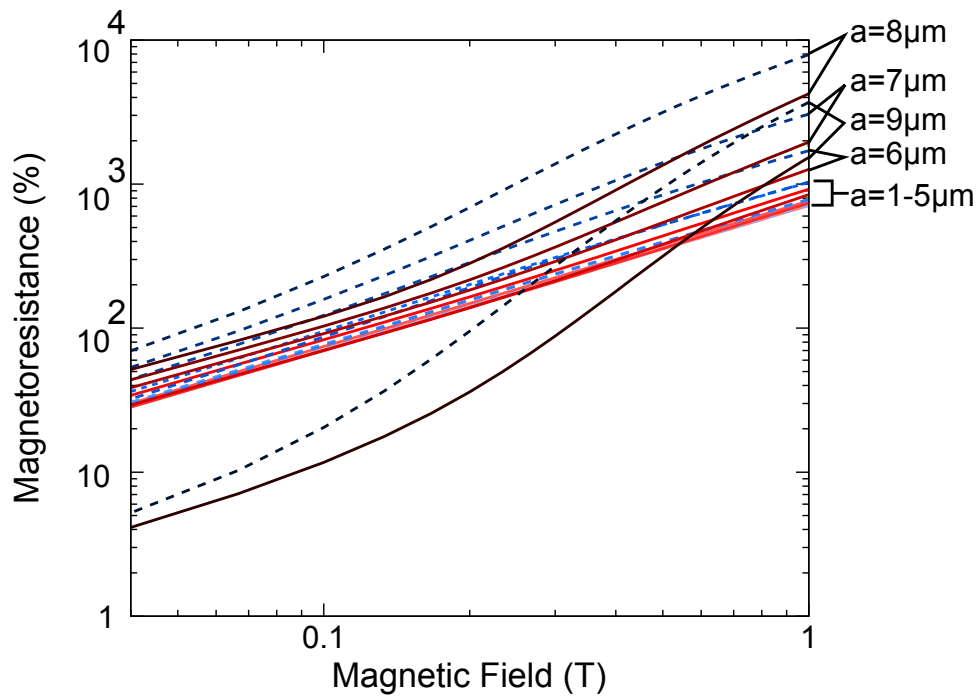


FIG. 21. Plots of the magnetoresistance versus the magnetic field for a $10 \mu\text{m}$ square with ports IVIV. The dashed lines represent the MR for negative values of the magnetic field.

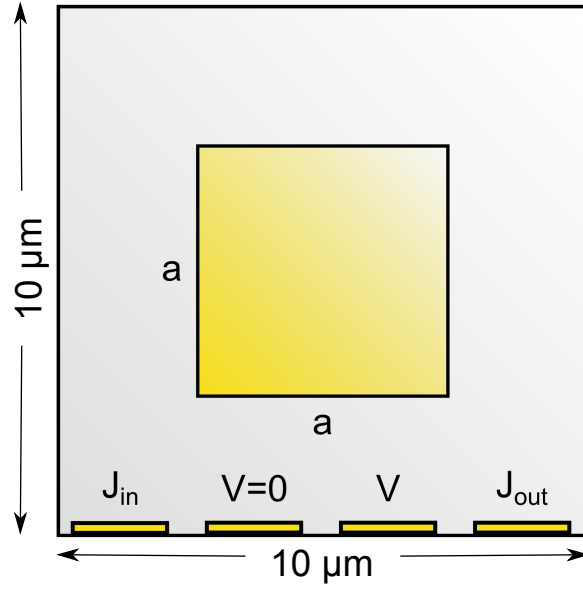


FIG. 22. A schematic for a $10\ \mu\text{m}$ square with ports IVVI.

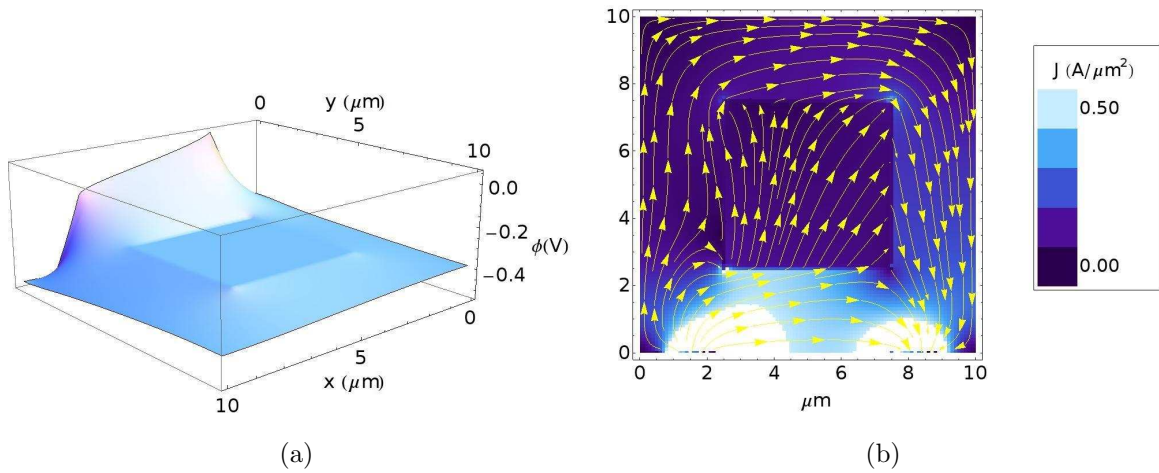


FIG. 23. The potential (a) and the plot of the current (b) for a $10\ \mu\text{m}$ square with ports IVVI with a $5\ \mu\text{m}$ metallic region and an applied field of $B = -1\ \text{T}$ is shown.

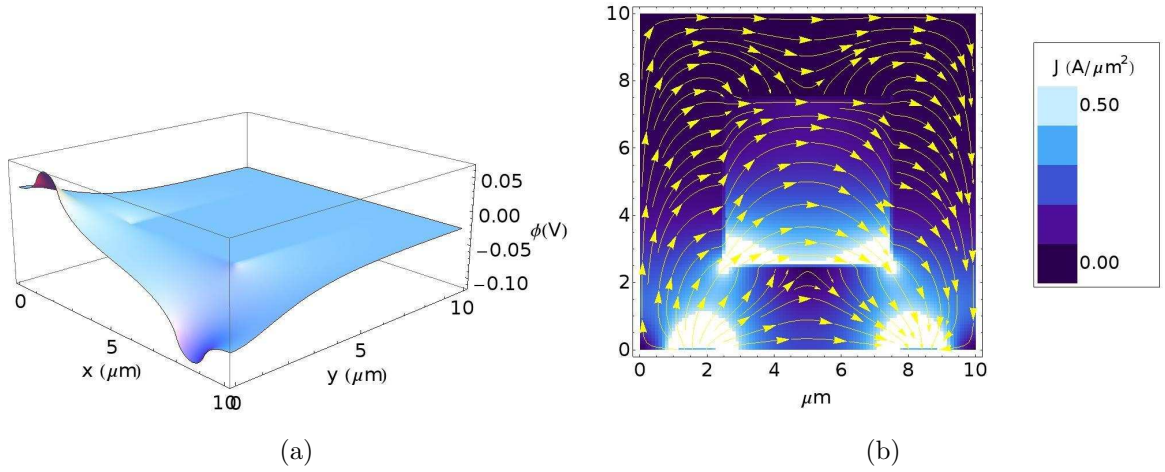


FIG. 24. The potential (a) and the plot of the current (b) for a $10\ \mu\text{m}$ square with ports IVVI with a $5\ \mu\text{m}$ metallic region and an applied field of $B = 0\ \text{T}$ is shown.

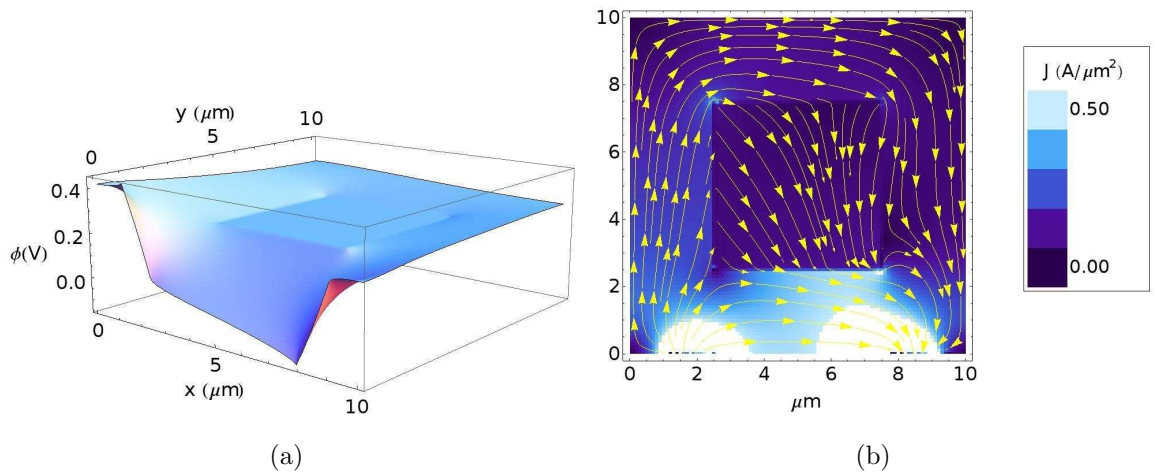


FIG. 25. The potential (a) and the plot of the current (b) for a $10\ \mu\text{m}$ square with ports IVVI with a $5\ \mu\text{m}$ metallic region and an applied field of $B = 1\ \text{T}$ is shown.

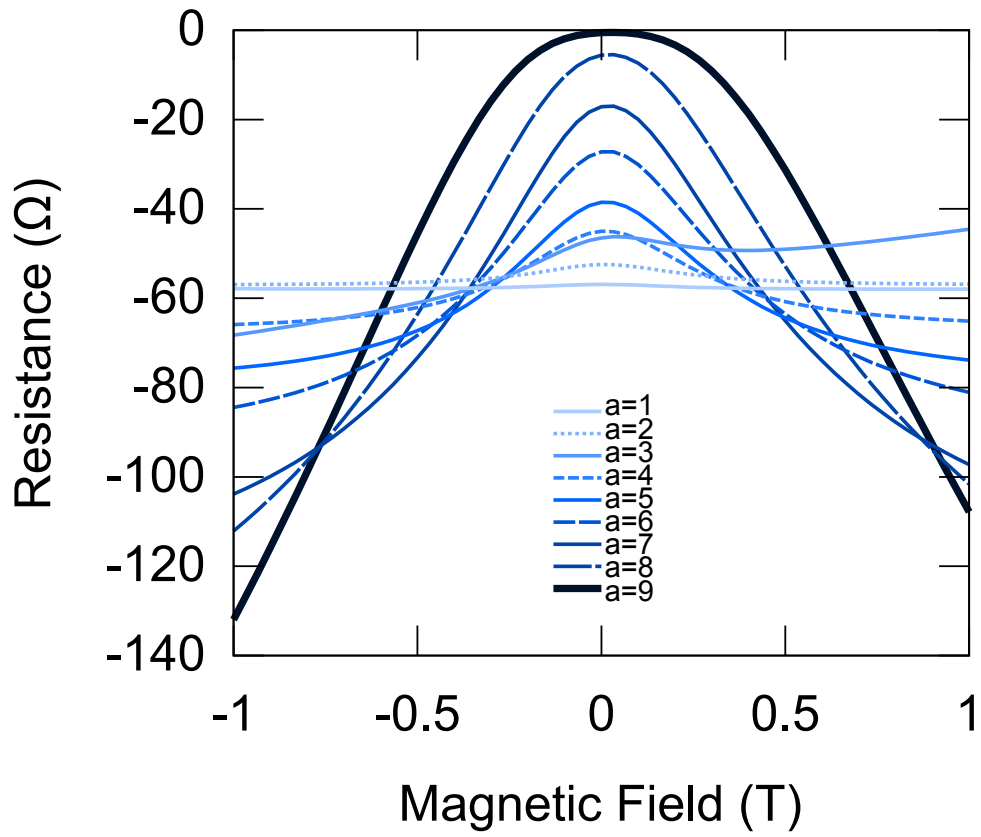


FIG. 26. Plots of the resistance versus the magnetic field for a $10\ \mu\text{m}$ square with ports IVVI. Note that an exchange of the voltage ports would lead to a positive resistance.

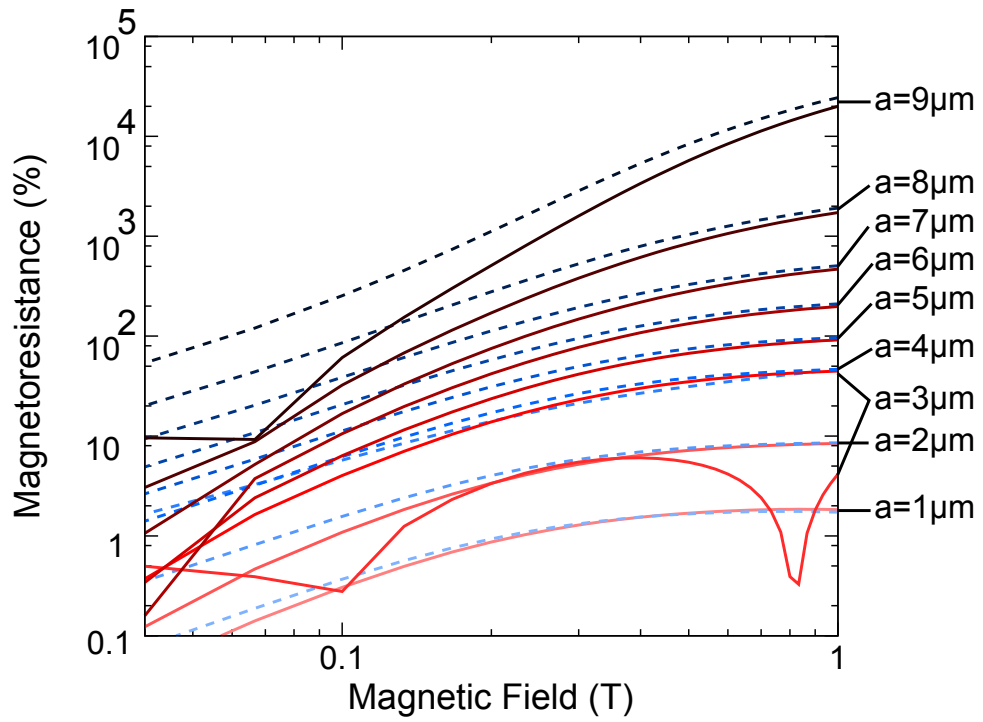


FIG. 27. Plots of the magnetoresistance versus the magnetic field for a $10\mu\text{m}$ square with ports IVVI. The dashed lines represent the MR for negative values of the magnetic field.

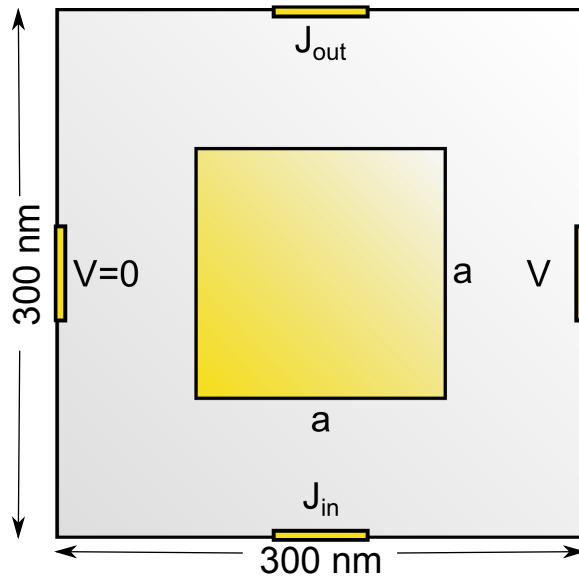


FIG. 28. A schematic for a 300 nm square with ports centered on all sides.

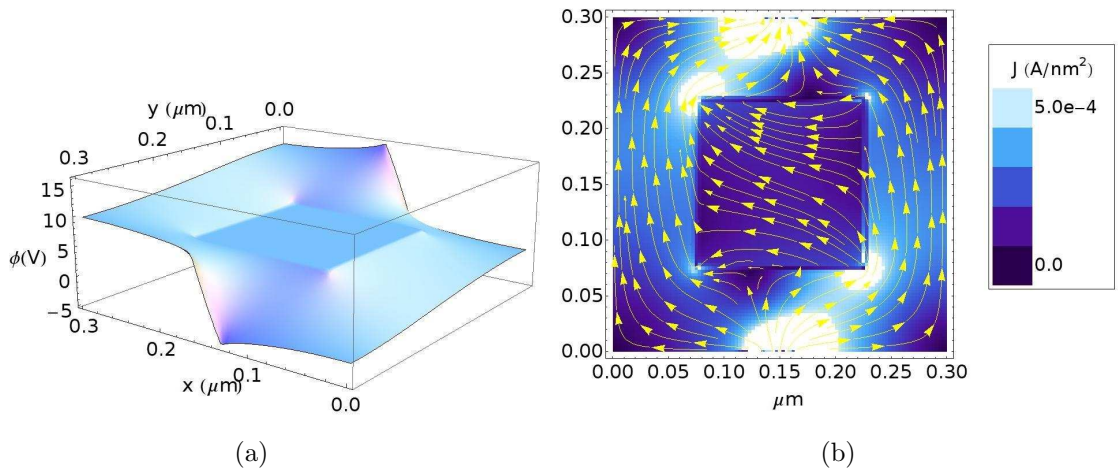


FIG. 29. The potential (a) and the plot of the current (b) for a 300 nm square with centered ports with a 150 nm metallic region and an applied field of $B = -1$ T is shown.

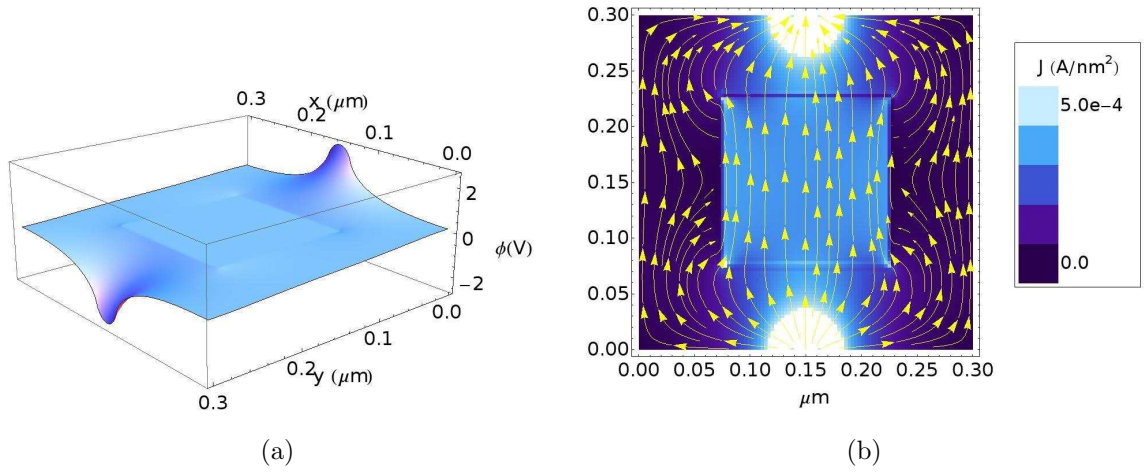


FIG. 30. The potential (a) and the plot of the current (b) for a 300 nm square with centered ports with a 150 nm metallic region and an applied field of $B = 0$ T is shown.

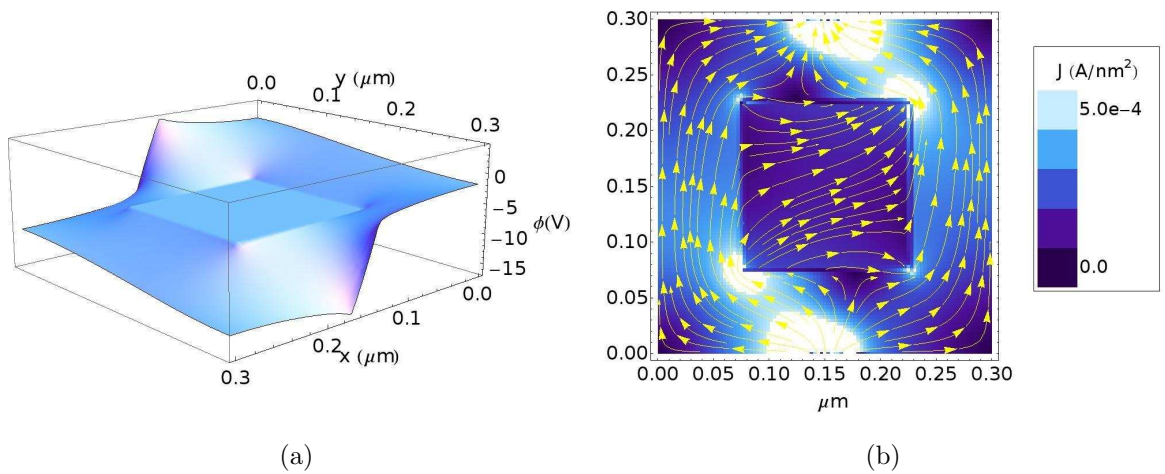


FIG. 31. The potential (a) and the plot of the current (b) for a 300 nm square with centered ports with a 150 nm metallic region and an applied field of $B = 1$ T is shown.

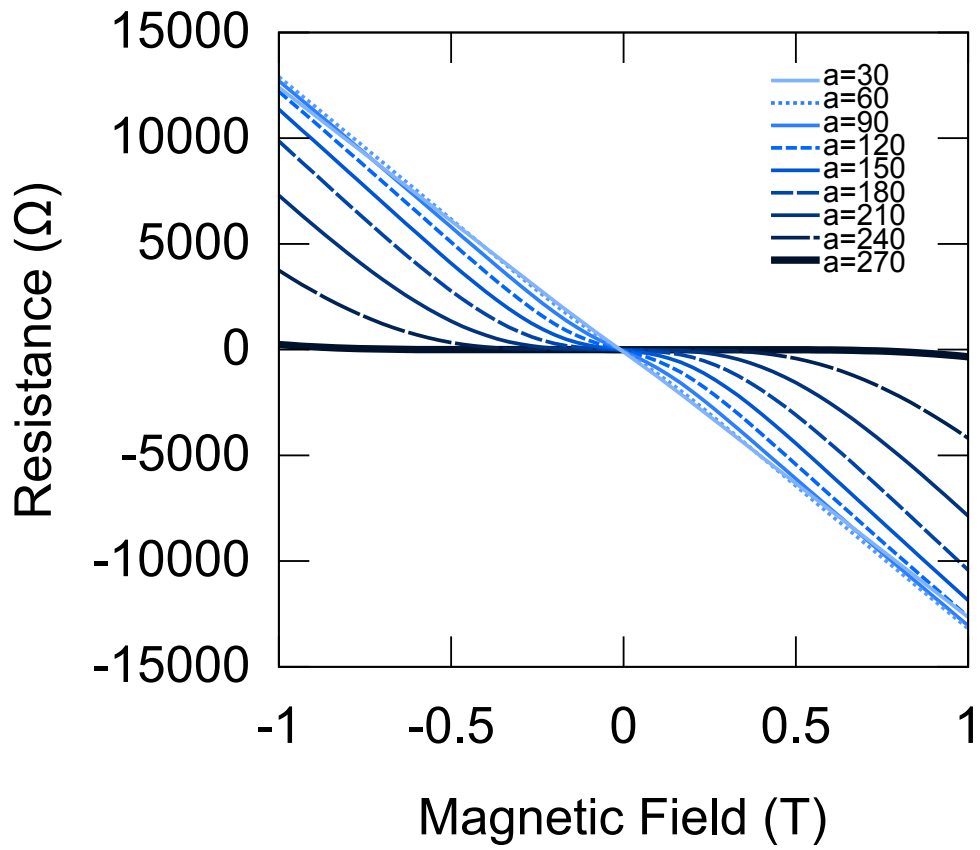


FIG. 32. Plots of the resistance versus the magnetic field for a 300 nm square with ports centered on all sides.

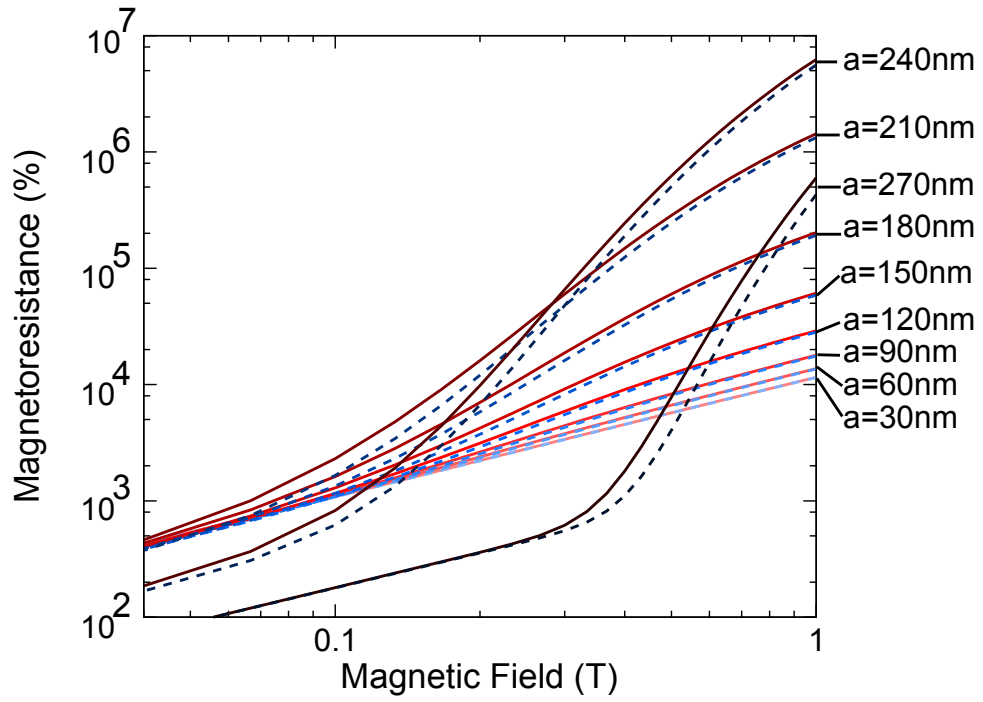


FIG. 33. Plots of the magnetoresistance versus the magnetic field for a 300 nm square with ports centered on all sides. The dashed lines represent the MR for negative values of the magnetic field.

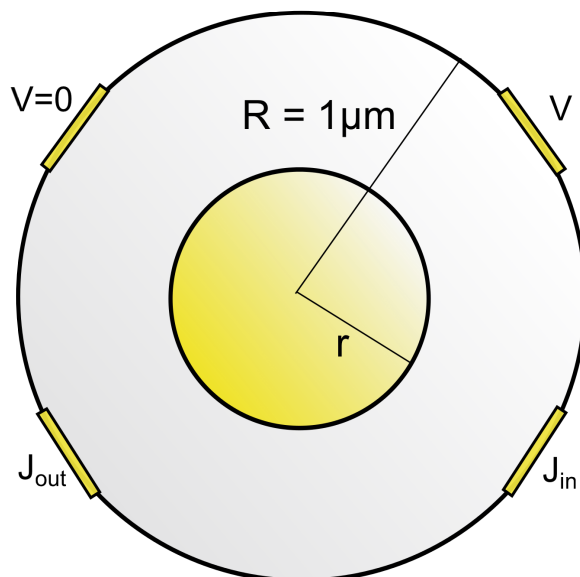


FIG. 34. A schematic for a $1\ \mu\text{m}$ circle with equally spaced contacts.

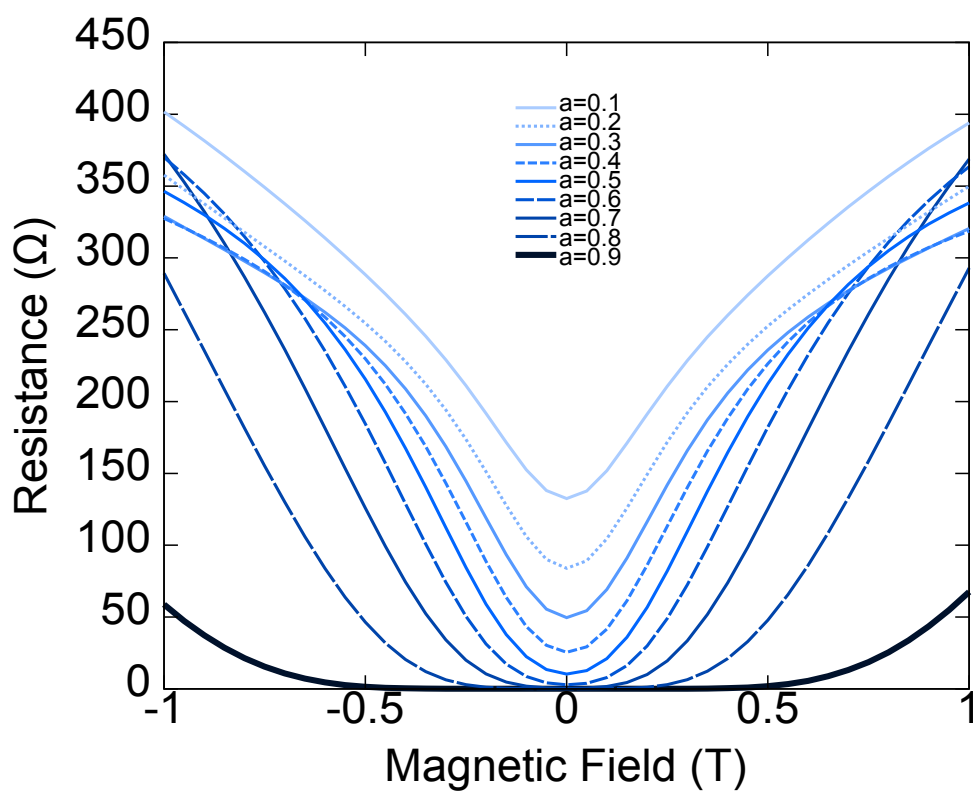


FIG. 35. Plots of the resistance versus the magnetic field for a $1\ \mu\text{m}$ circle.

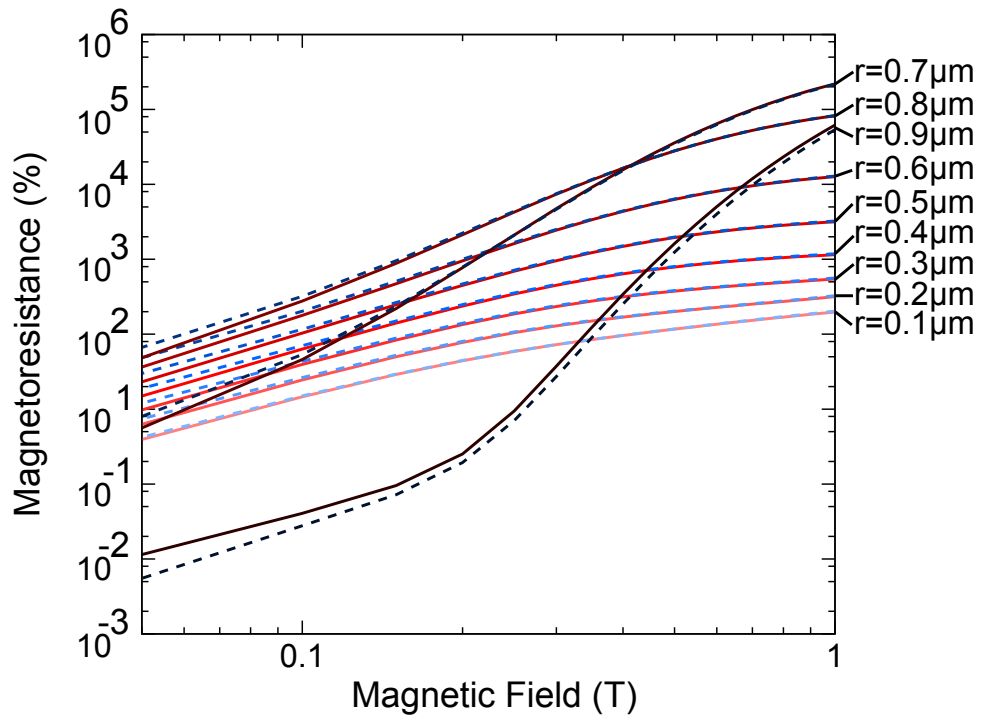


FIG. 36. Plots of the magnetoresistance versus the magnetic field for a 1 μm circle. The dashed lines represent the MR for negative values of the magnetic field.

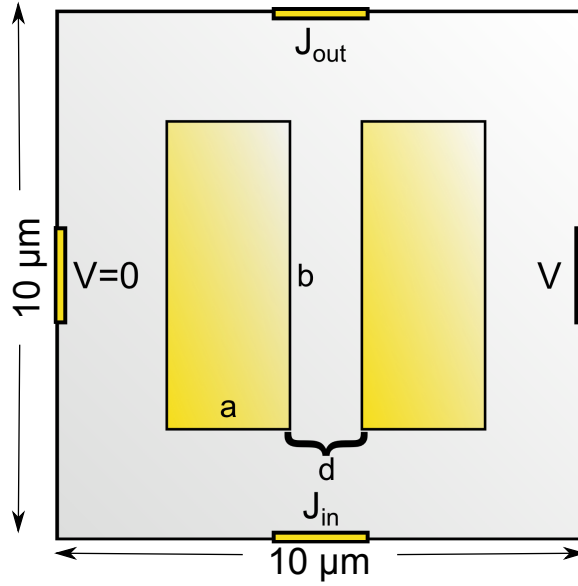


FIG. 37. A schematic for a $10\ \mu\text{m}$ square with two metal regions and current ports along x .

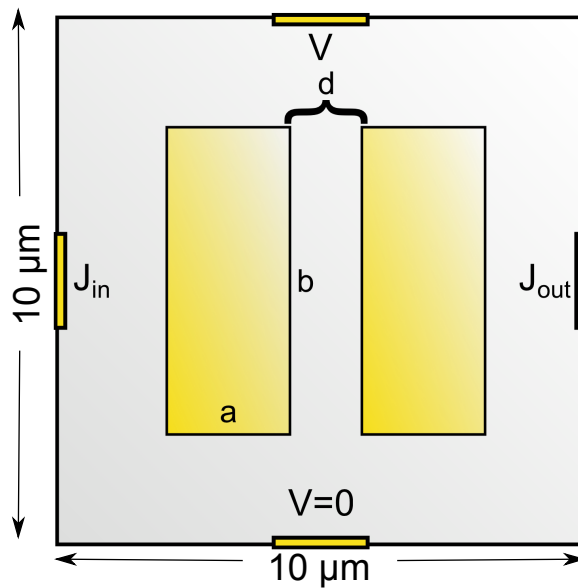


FIG. 38. A schematic for a $10\ \mu\text{m}$ square with two metal regions and current ports along y .

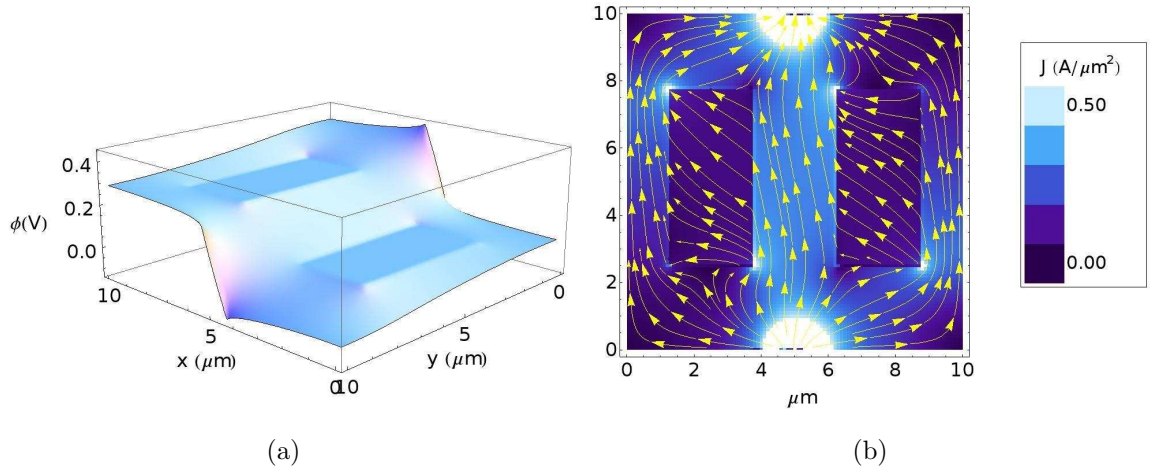


FIG. 39. The potential (a) and the plot of the current (b) for a $10\ \mu\text{m}$ square with centered ports along x with 2 metal regions and an applied field of $B = -1\ \text{T}$ is shown.

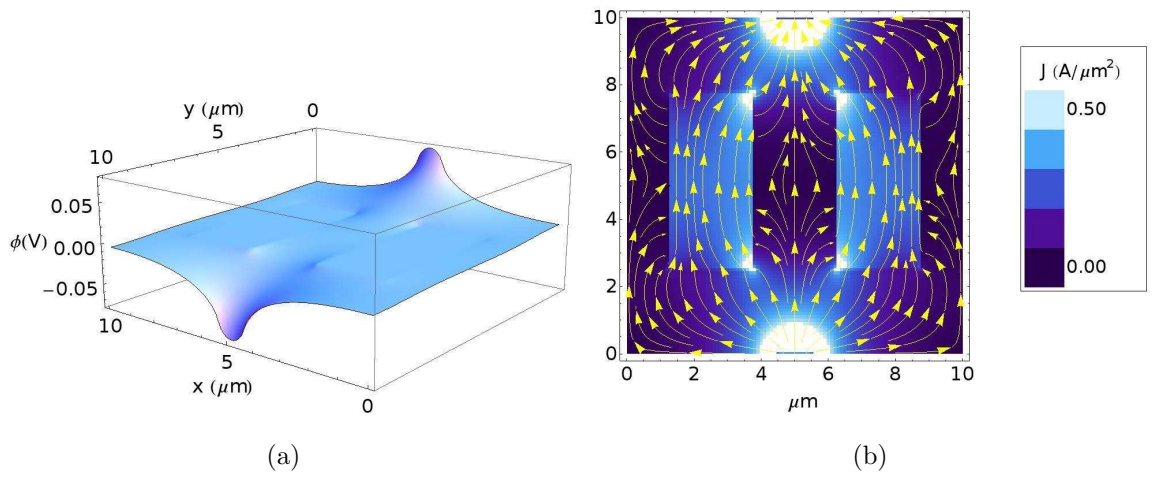


FIG. 40. The potential (a) and the plot of the current (b) for a $10\ \mu\text{m}$ square with centered ports along x with 2 metal regions and an applied field of $B = 0\ \text{T}$ is shown.

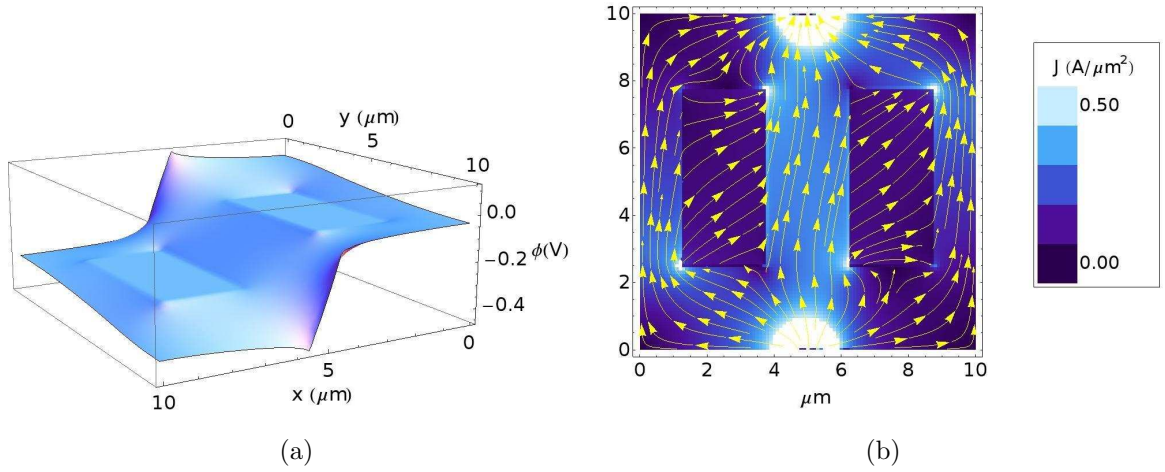


FIG. 41. The potential (a) and the plot of the current (b) for a $10\ \mu\text{m}$ square with centered ports along x with 2 metal regions and an applied field of $B = 1\ \text{T}$ is shown.

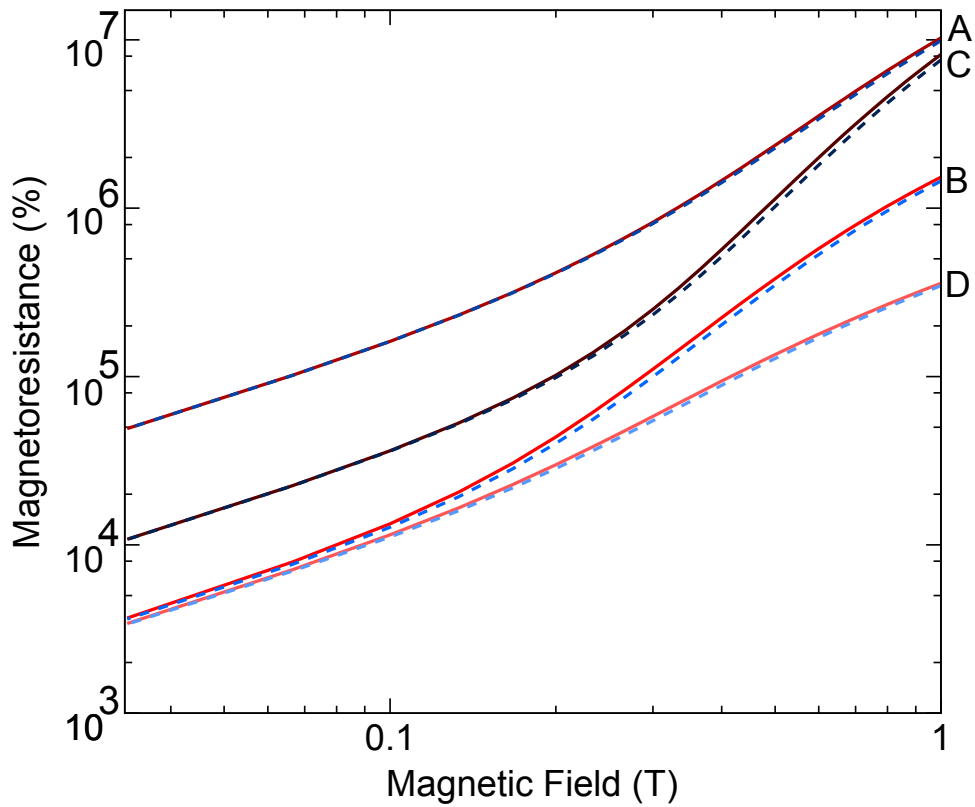


FIG. 42. Plots of the magnetoresistance versus the magnetic field for a $10\ \mu\text{m}$ square with 2 metal regions and ports centered along x . The dashed lines represent the MR for negative values of the magnetic field. Cases A,B,C,D are specified in the text.

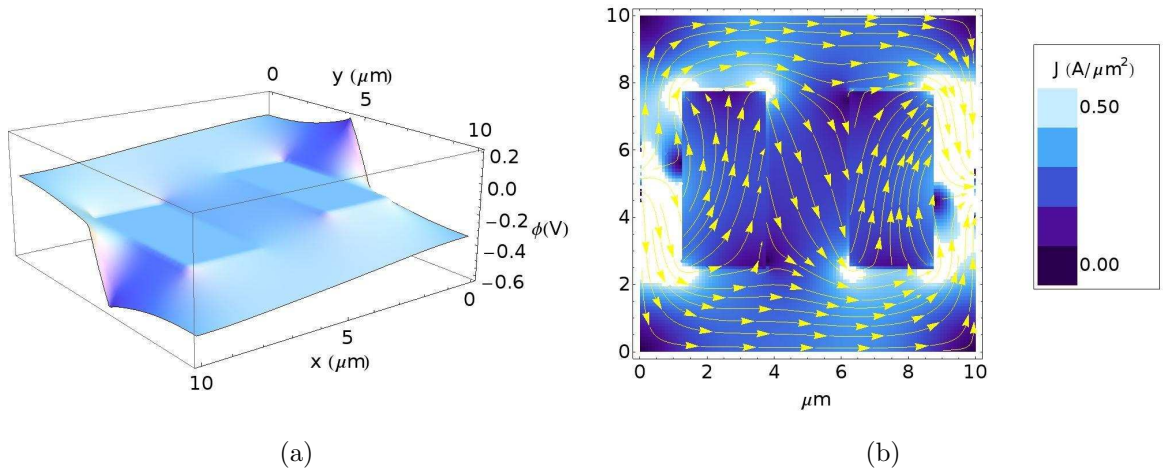


FIG. 43. The potential (a) and the plot of the current (b) for a $10\ \mu\text{m}$ square with centered ports along y with 2 metal regions and an applied field of $B = -1\ \text{T}$ is shown.

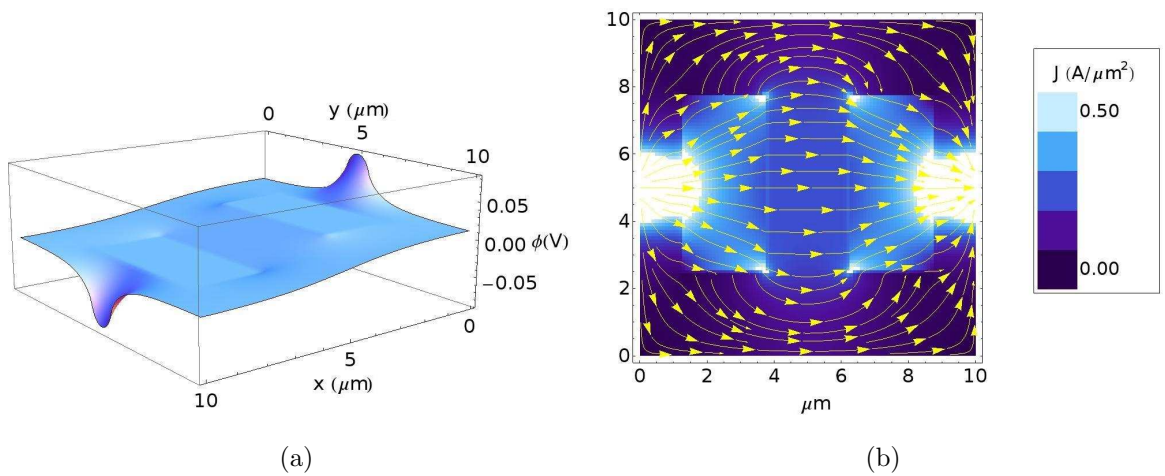


FIG. 44. The potential (a) and the plot of the current (b) for a $10\ \mu\text{m}$ square with centered ports along y with 2 metal regions and an applied field of $B = 0\ \text{T}$ is shown.

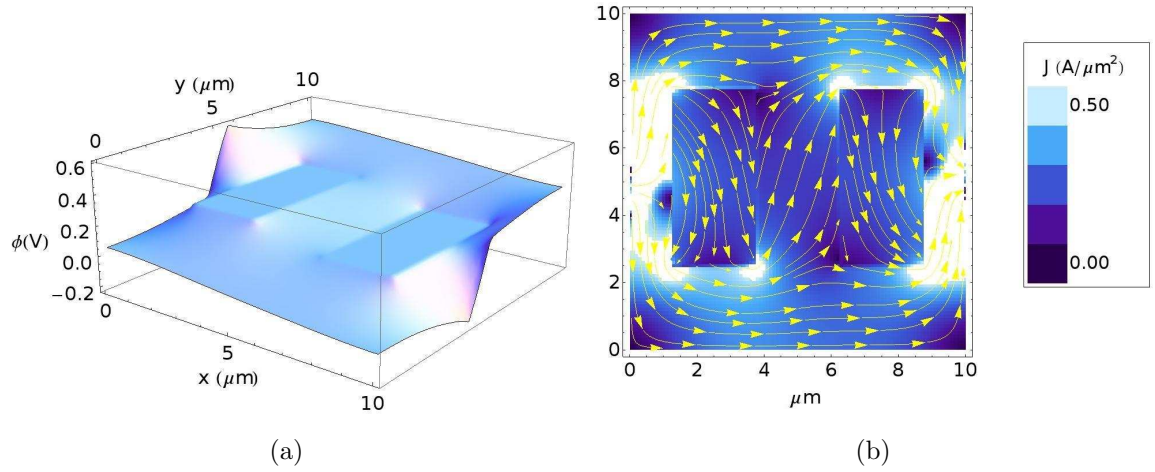


FIG. 45. The potential (a) and the plot of the current (b) for a $10\ \mu\text{m}$ square with centered ports along y with 2 metal regions and an applied field of $B = 1\ \text{T}$ is shown.

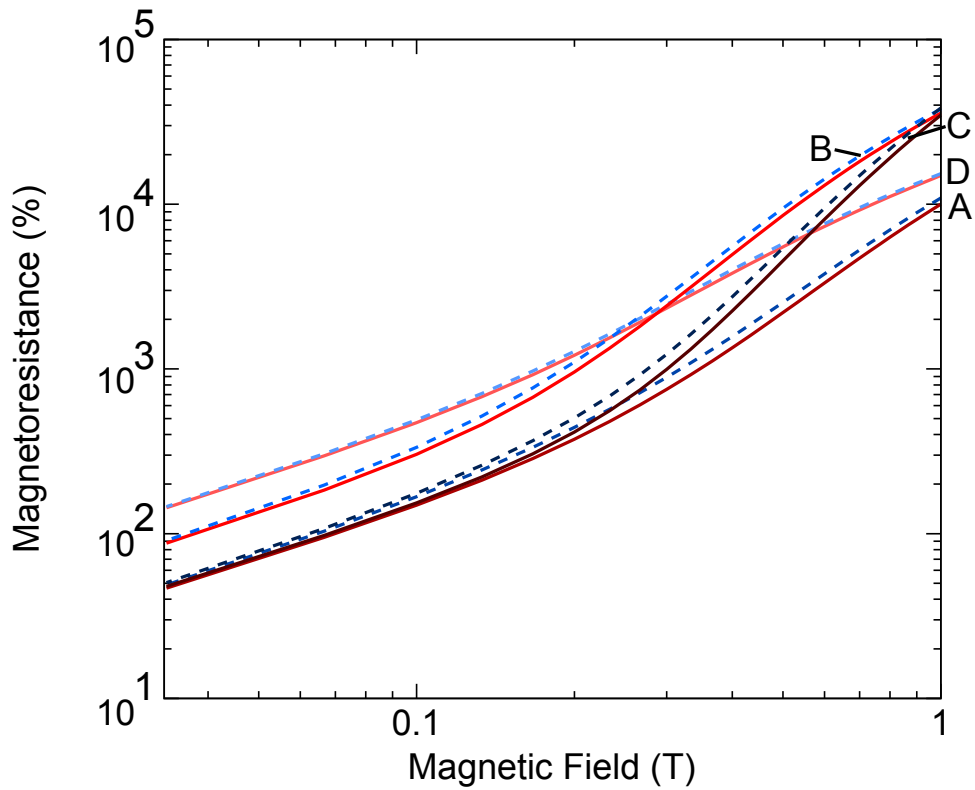


FIG. 46. Plots of the magnetoresistance versus the magnetic field for a $10\ \mu\text{m}$ square with 2 metal regions and ports centered along y . The dashed lines represent the MR for negative values of the magnetic field. Cases A,B,C,D are specified in the text.

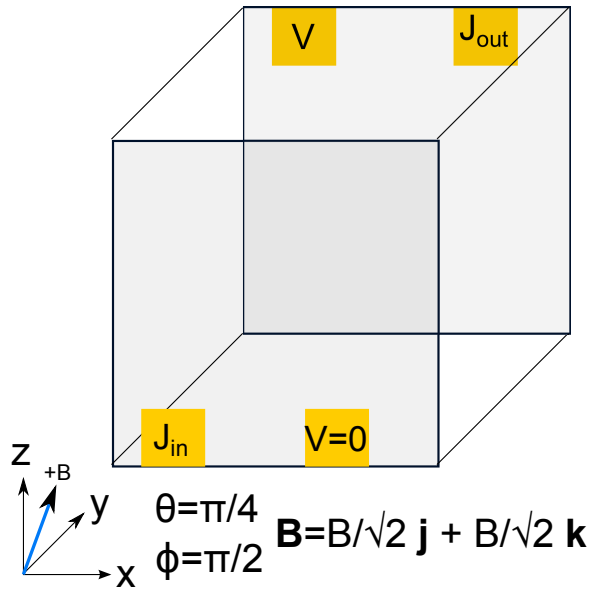


FIG. 47. A schematic for a $10 \mu\text{m}$ Cube with \vec{B} along y and z (Case 1). The semiconductor cube has an embedded metal cube which is centered within it.

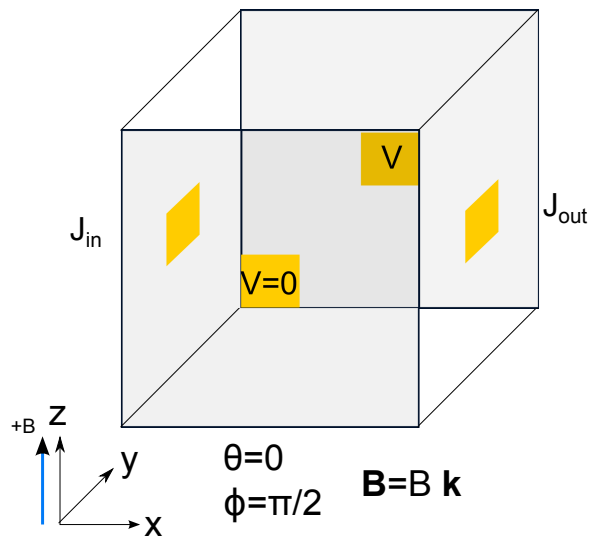


FIG. 48. A schematic for a $10 \mu\text{m}$ Cube with \vec{B} along z only (Case 2). The semiconductor cube has an embedded metal cube which is centered within it.

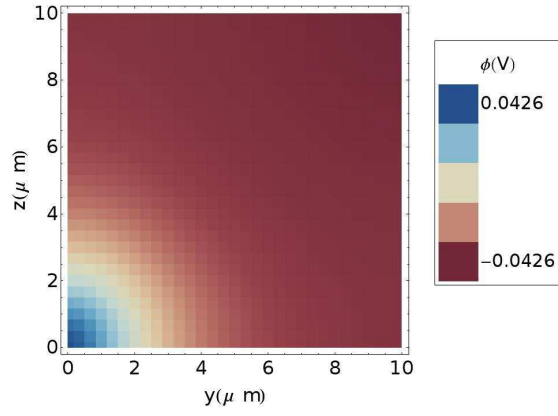


FIG. 49. Potential for the cube (case 1) along y - z plane for $x = 0 \mu\text{m}$ for $B = 0\text{T}$

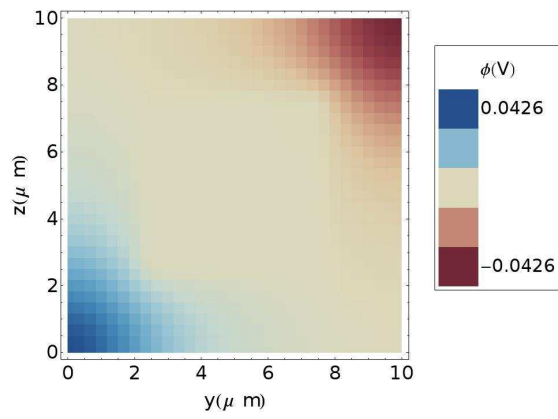


FIG. 50. Potential for the cube (case 1) along y - z plane for $x = 5 \mu\text{m}$ for $B = 0\text{T}$

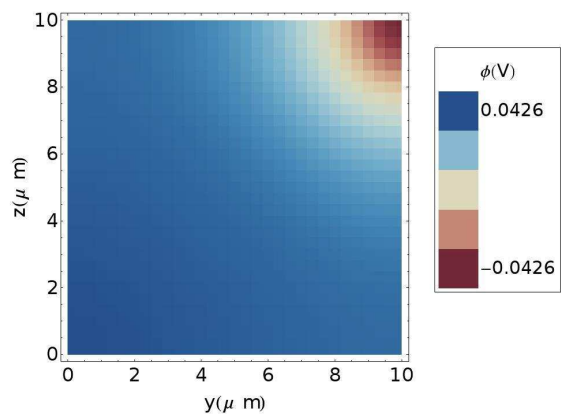


FIG. 51. Potential for the cube (case 1) along y - z plane for $x = 10 \mu\text{m}$ for $B = 0 \text{ T}$

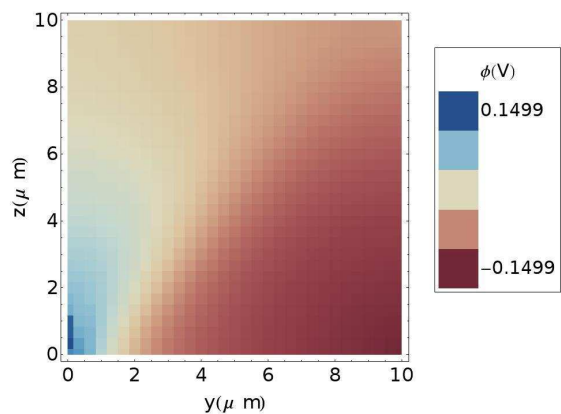


FIG. 52. Potential for the cube (case 1) along y - z plane for $x = 0 \mu\text{m}$ for $B = -1 \text{ T}$

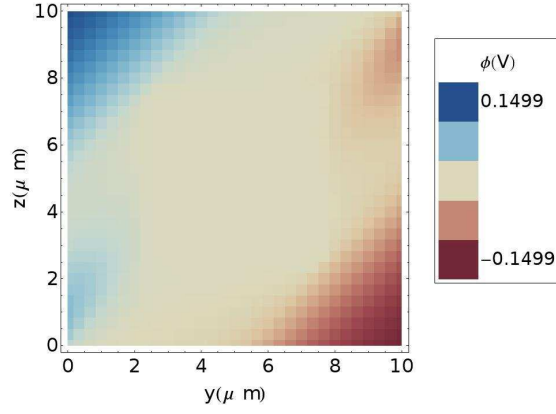


FIG. 53. Potential for the cube (case 1) along y - z plane for $x = 5 \mu\text{m}$ for $B = -1 \text{ T}$

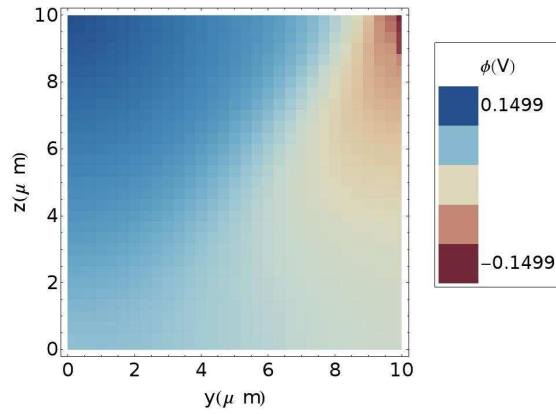


FIG. 54. Potential for the cube (case 1) along y - z plane for $x = 10 \mu\text{m}$ for $B = -1 \text{ T}$

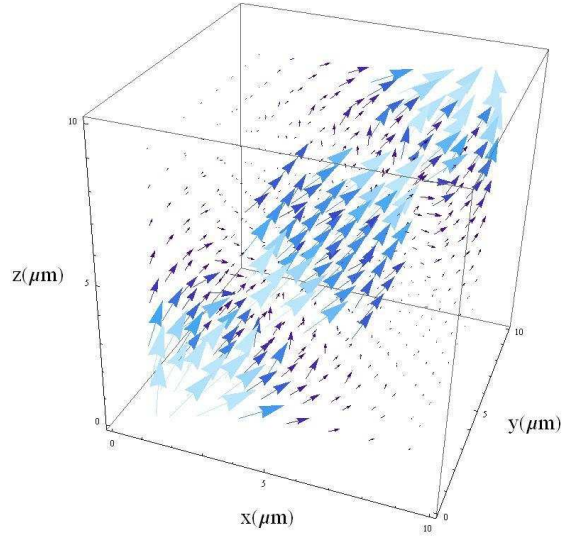


FIG. 55. Current plot for the cube (case 1) for $B = 0$ T

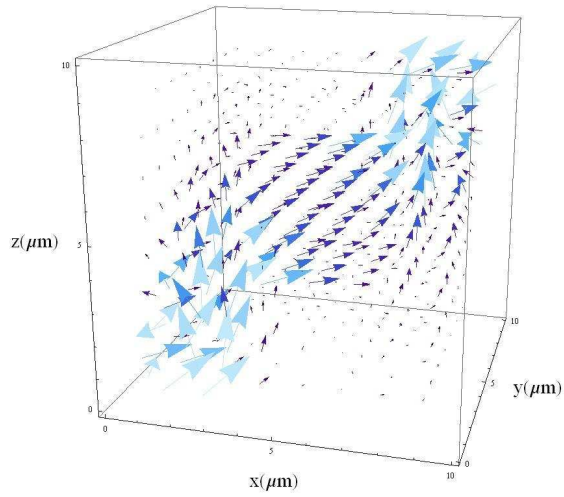


FIG. 56. Current plot for the cube (Case 1) for $B = -1$ T

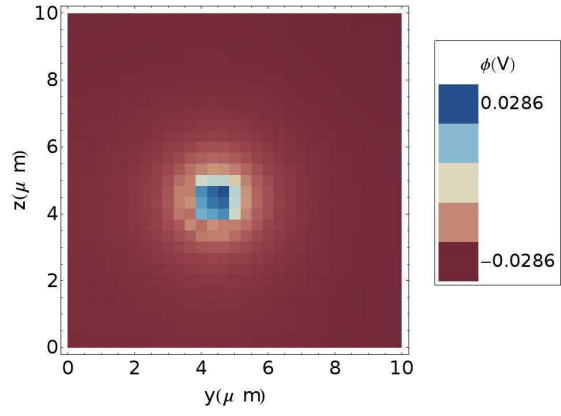


FIG. 57. Potential plot for the cube (Case 2) with $x = 0 \mu\text{m}$ for $B = 0 \text{T}$

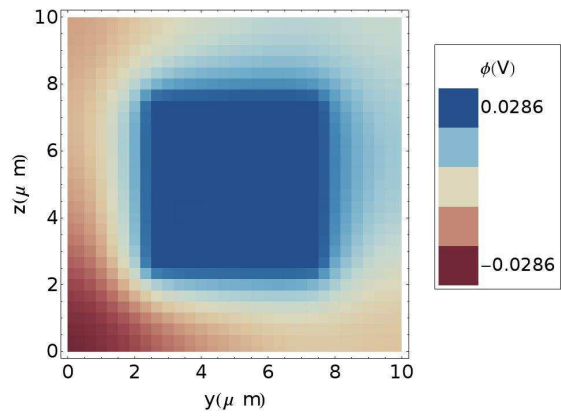


FIG. 58. Potential plot for the cube (Case 2) with $x = 5 \mu\text{m}$ for $B = 0 \text{T}$

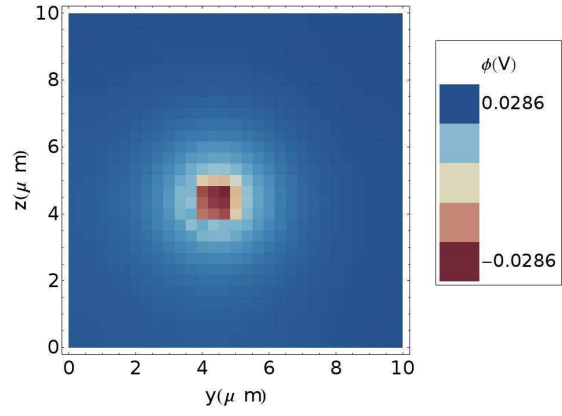


FIG. 59. Potential plot for the cube (Case 2) with $x = 10 \mu\text{m}$ for $B = 0 \text{ T}$

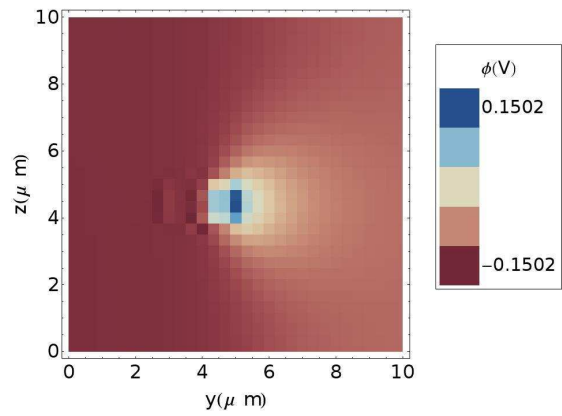


FIG. 60. Potential plot for the cube (Case 2) with $x = 0 \mu\text{m}$ for $B = 1 \text{ T}$

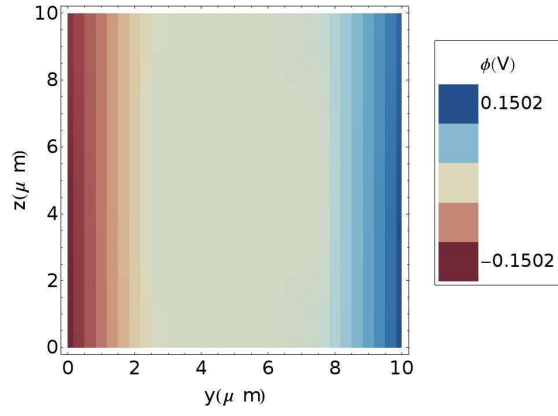


FIG. 61. Potential plot for the cube (Case 2) with $x = 5 \mu\text{ m}$ for $B = 1 \text{ T}$

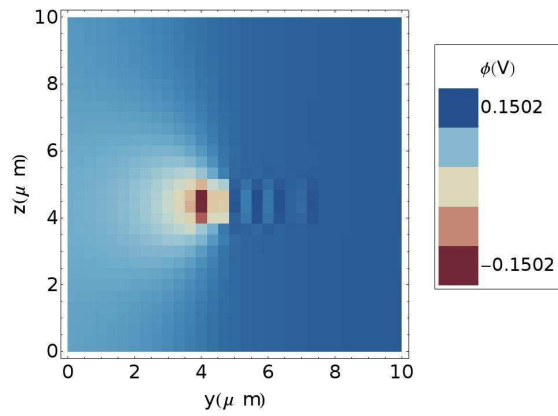


FIG. 62. Potential plot for the cube (Case 2) with $x = 10 \mu\text{ m}$ for $B = 1 \text{ T}$

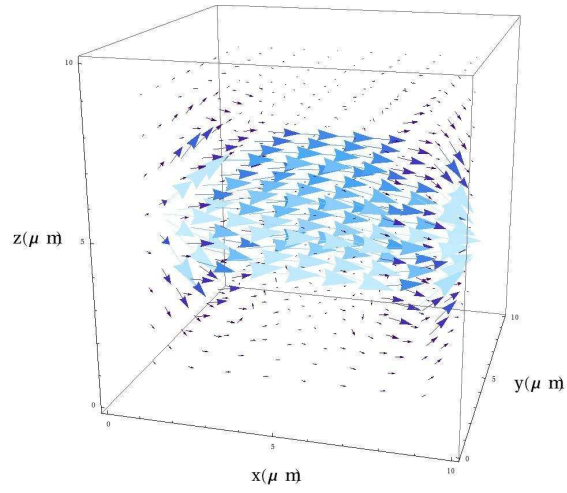


FIG. 63. Current plot for the cube (case 2) for $B = 0\text{ T}$

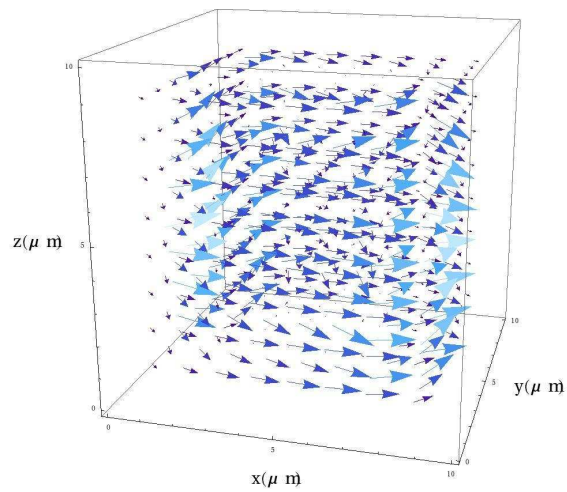


FIG. 64. Current plot for the cube (case 2) for $B = 1\text{ T}$

-
- ¹ S. A. Solin, Tineke Thio, D. R. Hines, and J. J. Hermans, *Science* **289**, 1530 (2000).
 - ² S. A. Solin, Tineke Thio, D. R. Hines, J. J. Heremans, and T. Zhou, Proceedings of the 25th International Conference on the Physics of Semiconductors, Osaka, Japan, edited by N. Miura (Springer, Berlin, 2001), pp. 1771-1774.
 - ³ T. Zhou, D. R. Hines, and S. A. Solin, *Appl. Phys. Lett.* **78**, 667 (2001).
 - ⁴ A. C. H. Rowe, K. Fasanella, T. Zhou, D. R. Hines, and S. A. Solin, *Rev. Sci. Instrum.* **73**, 4270 (2002).
 - ⁵ A. C. H. Rowe, D. R. Hines, and S. A. Solin, *Appl. Phys. Lett.* **83**, 1160 (2003).
 - ⁶ A. C. H. Rowe and S. A. Solin, *Phys. Rev. B* **71**, 235323 (2005).
 - ⁷ A. C. H. Rowe, A. Donoso-Barrera, Ch. Renner, S. Arscott, *Phys. Rev. Lett.* **100**, 145501 (2008).
 - ⁸ K. Wieland, Y. Wang, L. R. Ram-Mohan, S. A. Solin, and A. M. Girgis, *Applied Physics Letters* **88**, 052105-052108 (2005).
 - ⁹ K. Wieland, Y. Wang, S. A. Solin, A. M. Girgis, and L. R. Ram-Mohan, *Physical Review B* **73**, 155305-155312 (2006).
 - ¹⁰ K. A. Wieland, Yun Wang, S. A. Solin, A. M. Girgis, and L. R. Ram Mohan, 28th International Conference on the Physics of Semiconductors, Vienna, Austria, *AIP conf. Proc.* **893**, 1465 (2007).
 - ¹¹ Yun Wang, A. K. M. Newaz, Jian Wu, S. A. Solin, V. R. Kavasseri, N. Jin, I. S. Ahmed, and I. Adesida, *Appl. Phys. Lett.* **92**, 262106 (2008).
 - ¹² J. Moussa, L. R. Ram-Mohan, J. Sullivan, T. Zhou, D. R. Hines, and S. A. Solin, *Phys. Rev. B* **64**, 184410 (2001).
 - ¹³ R. S. Popovic, *Hall Effect Devices* (Adam Hilger, Bristol, 1991).
 - ¹⁴ S. Solin, D. R. Hines, A. C. H. Rowe, J. S. Tsai, Y. A. Pashkin, S. J. Chung, N. Goel, and M. B. Santos, *Appl. Phys. Lett.*, vol. 80, pp. 40124014 (2002).
 - ¹⁵ J. Moussa, L. R. Ram-Mohan, A. C. H. Rowe, S. A. Solin, *Journal of Applied Physics* **94**, 1110 (2003).
 - ¹⁶ S. A. Solin, *Sci. Am.* **291**, 70 (2004).

- ¹⁷ S. A. Solin and L. R. Ram-Mohan, Geometry-driven Magnetoresistance, in *Handbook of Magnetism and Advanced Magnetic Materials*, Edited by H. Kronmüller and S. Parkin, Volume **5**: Spintronics and Magnetoelectronics (John Wiley & Sons, NY, 2007); pp1-21.
- ¹⁸ L. R. Ram-Mohan, *Finite Element and Boundary Element Applications to Quantum Mechanics* (Oxford University Press, Oxford, 2002).
- ¹⁹ O. C. Zienkiewicz and R. L. Taylor, *The Finite Element Method*, 4th ed. (McGraw-Hill, New York, 1994); T. J. R. Hughes, *The Finite Element Method* (Prentice-Hall, Englewood Cliffs, NJ, 1987).
- ²⁰ R. Courant and D. Hilbert, *Methods of Mathematical Physics* (Interscience Publishers, New York, 1953).
- ²¹ M. Hoener, O. Kronenwerth, C. Heyn, D. Grundler and M. Holz, J. Appl. Phys. **99**, 036102 (2006).
- ²² M. Holz, O. Kronenwerth, and D. Grundler, Appl. Phys. Lett. **83**, 3344 (2003); Phys. Rev. B **67**, 195312 (2003); Appl. Phys. Lett. **86**, 072513 (2005).
- ²³ T. H. Hewett and F. V. Kusmartsev, Phys. Rev. B **82**, 212404 (2010).